Chemical Engineering Journal 481 (2024) 148189

Contents lists available at ScienceDirect

Chemical Engineering Journal

journal homepage: www.elsevier.com/locate/cej

A membrane's blueprint: *In silico* investigation of fluid flow and molecular transport as a function of membrane design parameters in organ-on-a-chip

P.D. Menezes, S. Hecht, A. Hunter, N. Gadegaard *

Division of Biomedical Engineering, James Watt School of Engineering, University of Glasgow, University Avenue, Glasgow G12 8QQ, United Kingdom

ARTICLE INFO

Keyword:
Finite element modelling
Membrane parameters
Microfluidics
Molecular concentration distribution
Organ-on-a-chip
Lab on chip

ABSTRACT

Following the rapid growth of Organ-on-a-Chip (OoaC) technology, porous membranes have become essential components for *in vitro* tissue barrier models. Nonetheless, literature highlights lacking knowledge on their integration and effect on microfluidic devices. Therefore, we conducted finite element modelling (FEM) to characterize the influence of membrane, channel geometry, flow and diffusion parameters, in modelling flow rate, shear stress, transient transport and steady state molecular concentration. This analysis was performed for four different conditions based on single channel (*SCP*) and parallel perfusion (*PP*). It was found that membrane and geometry parameters are crucial in determining flow and shear for *SCP*. However, for *PP*, flow and shear are predominantly governed by the inlet flow rate. Although the transient behaviour is well-controlled within *SCP* and *PP*, only *PP* allows modelling the steady state concentration distribution. It is highlighted that: (1) the pore radius has great influence on flow and shear; (2) a shallow cell channel and a long membrane are capable of establishing different levels of shear on opposing surfaces of the same channel; (3) the membrane thickness, membrane length, height of the cell and flow channels, and inlet flow rate provide good control over transient transport; (4) the membrane length and inlet flow rate enable changing the concentration from a uniform distribution to a complete heterogeneous state across the device. Experimental assays were performed to support the FEM and evidence its significance for OoaC applications. Ultimately, extensive, and systematic guidelines are provided on designing future OoaC devices with integrated porous membranes.

1. Introduction

Reproducing human physiology *in vitro* has long captured the attention of science and research, given its formidable potential to revolutionize biological research and healthcare [1]. About a century ago, the work of Harrison et al. [2] pioneered two-dimensional (2D) cell culture. Since then, growing efforts in biotechnology focus on the development of human tissue models of greater physiological relevance. This pursuit is notably urgent in the pharmaceutical industry, where despite great investments, the output of new drugs has remained mostly stagnant, resulting in a "productivity crisis" [3,4] with 89 % of new drugs failing clinical trials due to unpredicted human toxicity [5]. The lack of physiologically relevant preclinical models contributes to this inefficiency [6], given that neither static cell cultures nor animal models recapitulate the complex 3D constructs of human tissue and organs [7]. Indeed, there is a demand to develop novel methods for modelling human physiology and pathology [8].

Perhaps one of the most promising technologies addressing the present challenge is Organ-on-a-Chip (OoaC) [9–11]. These are microfluidic devices reliant on continuously perfused channels to culture living tissue and establish physiologically relevant *in vitro* models of human organs [12–16]. Their microscale explores the benefits of laminar fluidics to provide unparalleled control of key physiological parameters, such as chemical delivery [17] and fluid shear [18]. Furthermore, microfabrication techniques enable the integration of sensors, for monitoring and analysis, as well as mechanical, electrical and biochemical stimuli, to mimic extracellular cues as found *in vivo* [19–22]. Research in the field has already lead to the development of liver [23–26], heart [27,28], kidney [29], stomach [30], gut [31,32], muscle [33], bone [34], blood vessel [35,36], blood–brain-barrier [37], neuronal networks [38], retina [39] and placenta [40] OoaCs. Despite the great potential and existing applications, initiatives such as Organ-on-Chip In Development (ORCHID) highlight a subsisting necessity towards achieving greater physiological relevance and complexity [41–43].

The implementation of porous semi-permeable membranes has

* Corresponding author at: Division of Biomedical Engineering, University of Glasgow, Rankine Building, Oakfield Avenue, Glasgow G12 8LT, United Kingdom
E-mail address: nikolaj.gadegaard@glasgow.ac.uk (N. Gadegaard).

https://doi.org/10.1016/j.cej.2023.148189
Received 5 May 2023; Received in revised form 4 December 2023; Accepted 18 December 2023
Available online 21 December 2023

become an essential feature in any multi-compartment OoaC device [44]. It partitions the cellular microenvironment into connected chambers through which media and biochemical delivery can be achieved [45], this way, enabling co-culture and a superior emulation of *in vivo* tissue constructs, such as the gut epithelium, lung and liver. Membranes can be tuned to not only protect cells from direct shear flow, a factor widely known to influence cell differentiation, morphology and function [46–50], but also enable osmotically driven processes, by defining porous flux of solutes and solvents as a function of the membrane's permeability [51,52]. Beyond establishing a consistent 2D plane for better imaging, membranes can also contribute to the development of high-throughput screening assays [53] and long-term maintenance of co-culture systems [54]. This wide range of benefits makes porous semi-permeable membranes nearly transversal components to achieving greater physiological emulation in OoaC.

The integration of membranes into microfluidic devices is, however, not a trivial task. Beyond the manufacturing challenge they present, finding the right properties to ensure a specific fluidic and biochemical output, is subject of continuous research and consideration. The intrinsic properties of the membrane, such as porosity, pore radius and membrane thickness, are known to contribute to modelling porous flow [49] and molecular transport [45]. The morphology of pores contributes to changing the permeation of the membrane [55], and may promote electroosmotic flow, for dual pole nanopores [56]. Surface charge of the membrane is also an important factor, capable of stimulating molecular transport [57]. Beyond the membrane, external factors, such as the channel dimensions and geometry are critical to control fluid flow through the channels and across the membrane [50]. Changing the pH of the media, is also known to influence transport and delivery of molecules through the membrane [58].

Efforts to understanding and characterizing the implications of membrane parameters have led to several studies in the past decade. Analytical models first paved the way to simulating the fluidics and mass transport across simple membrane models [45,49,59]. Numerical modelling, with FEM, further expanded research on porous membranes, where dominant design parameters were investigated to characterize their effect on both the fluidics and shear [50], as well as the transient behaviour of molecular transport [54], within microfluidic bilayer devices. Porosity and membrane thickness have also been numerically investigated, to obtain solutions to the Nernst-Planck equations and characterize the transfer of acidic and basic drugs in electromembrane extraction [60]. More advanced parameters, such as the morphology of pores, have also been analysed under FEM, quantifying their effect on electroosmotic flow and transport [55,56]. Despite the substantial amount of research, and reviews published in parallel [44,61], literature is clear in emphasising a subsisting 'lack of criteria for membrane porosity selection and channel size design' [50] when it comes to defining the fluidics and molecular transport of general microfluidic platforms, calling for a broader, more systematic investigation [44,54].

Aiming to address this gap, the present study employs FEM to describe the direct relationship between response variables and control parameters, by providing individual functions for each of the 288 combinations tested within a microfluidic bilayer design with integrated porous membrane. Design parameters, namely porosity, pore radius, membrane thickness, membrane length, channel heights, inlet flow rate and diffusion coefficient rate, were extensively investigated within a range of 7 distinct data sets, and for a total of 4 different fluidic setups, characterizing both single channel perfusion and parallel perfusion. In turn, systematic analysis was carried out for each single combination, addressing the steady state fluid flow, wall shear stress, and molecular concentration distribution, as well as the transient rate of convective-diffusive transport of molecules across the membrane. Altogether, the present study provides unique guidelines, unmet by previous literature, extensively describing the individual relationships between design parameters and response variables, ultimately aiming to serve as foundational knowledge to design, select, and characterize porous membrane microfluidics. The respective modelling data has been further corroborated by *on-chip* fluorescent and biological experiments.

2. Methods

2.1. Geometric model

The present study focuses on simulating a generalized model of a microfluidic bilayer device with an integrated porous membrane, as illustrated in Fig. 1 a). Its design contemplates the basic elements of most common OoaC devices for tissue barrier simulation, hence including two adjacent channels separated by a porous membrane [40,62–65]. At the bottom, the flow channel (*FC*) takes on the role similar to that of blood vessels, allowing for independent flow of oxygen, nutrients and drugs. On the top, the cell channel (*CC*) provides the site for culture of cells. At the same time the porous membrane (*PM*) acts as an artificial *in vitro* endothelial barrier [66], confining convective transport to perfused channels, whilst enabling diffusive transport between compartments and providing mechanical support for cell growth.

Simulations were carried out in COMSOL Multiphysics v6.0, using a 2D FEM model, as illustrated in Fig. 1 b), to avoid unnecessary computational expenses associated with 3D modelling. The model was parametrically defined. This way, all initial conditions and design parameters are fully adjustable, enabling their impact on fluid flow, Q, and the molecular concentration distribution, C.

2.2. Numerical models

Two fundamental modules, available in COMSOL, were implemented to solve the fluid dynamics along the channels and through the membrane, as well as the transport of diluted molecules by the effect of both advective and diffusive mechanisms. The modules are respectively designated as *Porous Media Flow* and *Transport of Diluted Species*.

The *Porous Media Flow* module solves fluid flow in both free and porous media, which in the case of the present device, is represented by the flow along the channels and across the porous membrane respectively. First, to ensure both the conservation of momentum and mass, the Navier-Stokes and the Continuity equations [67] are respectively engaged. The Navier-Stokes equation is defined as follows:

$$\rho(\mathrm{u}\bullet\nabla\mathrm{u}) = -\nabla\bullet p\mathrm{I}+\nabla\bullet\left[\mu\left(\nabla\mathrm{u}+(\nabla\mathrm{u})^{T}\right)-\frac{2}{3}\mu(\nabla\mathrm{u})\mathrm{I}\right]+\rho\mathrm{F} \tag{1}$$

Where ρ [kg/m^3] is the fluid density, u [m/s] is the velocity vector, p [Pa] is the fluid pressure, I is the identity matrix, μ [Pa.s] is the fluid dynamic viscosity and F [N/kg] are the volume forces per unit mass of fluid. On the other hand, the Continuity equation is defined as follows:

$$\nabla\bullet(\rho\mathrm{u}) = 0 \tag{2}$$

Both equations are coupled together to solve for the free-flowing laminar motion of media being perfused into the microchannels of the device.

To calculate the flow of media across the membrane, described as slow flow through the interstices of a fully saturated medium, Darcy's Law must be engaged. The equation is formulated as follows:

$$v = \frac{K_m}{\mu L}\nabla p \tag{3}$$

Where v [m/s] represents instantaneous flux, L [m] the length of the porous medium (also here represented as a thickness, t_M, when the porous medium is considered as a membrane) and K_m [m^2] the hydraulic permeability of the membrane. The permeability is a property of a porous medium which quantifies its ability to transmit fluids across. It can be defined by the following expression [49,65]:

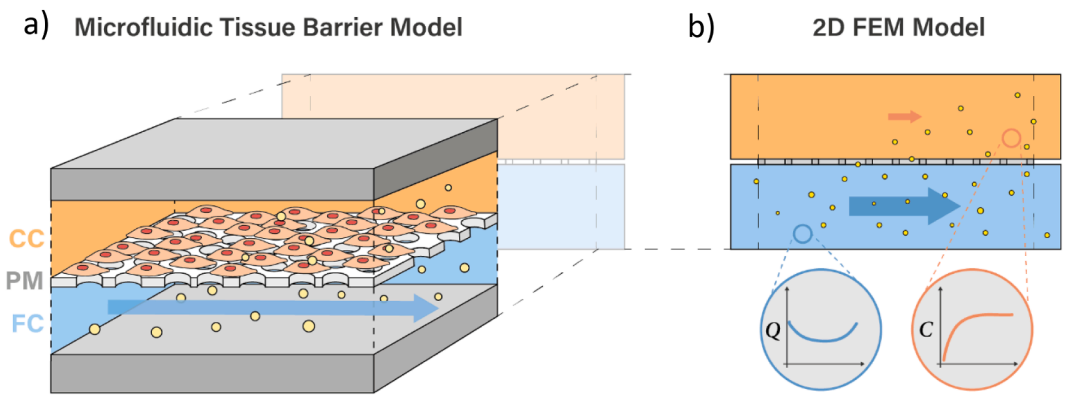

Fig. 1. . (a) 3D illustration of a microfluidic bilayer device with an integrated porous membrane subdividing the domain into the CC (cell channel) and FC (flow channel), b) 2D representation of the same device, illustrative of the geometry employed for FEM, from where data on Q (flow rate) and C (concentration) will be measured, analysed, and investigated.

$$K_m = \frac{\mu L P}{\pi r^2 R_{pore}} \tag{4}$$

Where r [m] is the pore radius, R_{pore} [kg/(m^{4}s)] the pore resistance and P the porosity of the medium. Porosity is defined as the fraction of surface area covered by pores. To define pore resistance though, it is first necessary to specify the nature of the porous medium which, in this case, is a thin, porous membrane. For this particular situation, pore resistance is more accurately defined by Dagan's equation, to account for entrance/exit effect of flow through a short through pore. Pore resistance, for a single pore, is then defined as follows [44]:

$$R_{pore} = \frac{\mu}{r^3}\left[3 + \frac{8}{\pi}\left(\frac{L}{r}\right)\right] \tag{5}$$

The *Transport of Diluted Species* module solves the motion of diluted particles flowing within the bulk media, by activating and coupling the transport mechanisms of advection and diffusion, expressed by the Advection-Diffusion equation. This equation derives from Brownian motion and Fick's law [68], and is expressed as follows:

$$\mathrm{u}\nabla C - D\nabla C = s(x,t) \tag{6}$$

Where C [mol/m^3] represent concentration, D [m^2/s] the diffusion coefficient and $s(x,t)$ [mol/(m^{2}s)] a source or sink of the respective diluted species for a specific x [m] position along the channel and at a certain time, t [s]. Whereas the first term of the equation, u∇C, represents the advection component, the second, $D\Delta C$, represents the diffusion. However, the presence of a porous medium, such as a membrane, imposes constraints to diffusion, which must be considered. These constraints can be translated by applying the Millington and Quirk model, which correlates porosity with tortuosity, τ, the latter defined as the ratio between the effective path length of the pore and the straight distance across the porous medium. This way, the notion of effective diffusivity, D_{eff} [m^2/s], is formulated, and can be expressed by the following expression:

$$D_{eff} = \frac{P}{\tau} D \tag{7}$$

2.3. Design parameters

2.3.1. Control parameters

Eight distinct control parameters, namely porosity, P, pore radius, r [μm], membrane thickness, t_M [μm], membrane length, L_M [mm], cell channel height, H_{CC} [μm], flow channel height, H_{FC} [μm], inlet flow rate, Q_{in} [μL/h], and diffusion coefficient rate, D [m^2/s], were individually analysed over a defined interval of values. These intervals were defined based on literature references and commercial examples. To facilitate the analysis of results, parameters were grouped into three distinct categories, namely the membrane properties, channel geometry, and flow and diffusion parameters. Each parameter was studied across a defined range, and given an initial value (bold face), as detailed in Table 1. When a parameter is being investigated over its respective range of values, all other parameters are fixed at their initial values. All the control parameters in the analysis are illustrated in Fig. 2.

2.3.2. Fluidic setup

To contemplate the multitude of fluidic architectures common to OoaC technology, four distinct fluidic conditions were analysed, as demonstrated in Fig. 3. These can be divided first into single channel perfusion, *SCP* (Fig. 3 a) and b)), and parallel perfusion, *PP* ((Fig. 3) and d)). Within *SCP*, the cell channel was either treated as a reservoir, SCP_R (Fig. 3 a)), for media flow and molecule transport, or as an outlet, SCP_O (Fig. 3 b)). It means that, for both conditions, flow in the *CC* is always a function of both K_M and volumetric flow in the flow channel, Q_{FC}. On the other hand, in *PP*, both the *CC* and the *FC* have independent media perfusion. Two conditions were similarly modelled within *PP*, which can be differentiated by the direction in which media perfusion is done. Either in the same direction, for PP_{SD} (Fig. 3 c)), or in the opposite direction, for PP_{OD} (Fig. 3 d)).

Table 1
. Investigated control parameters (CP), with their respective intervals of study and default values, highlighted in bold face. The values highlighted in bold with a * represent a default value which are not part of the interval of study.

CP	Designation	Interval of Study
P	Porosity	[0.001; 0.01; **0.1**; 0.2; 0.3; 0.4; 0.5; 0.6; 0.7; 0.8; 0.9]
R [μm]	Pore Radius	[0.001; 0.005; 0.01; 0.05; 0.1; 0.5; **1**; 5; 10; 50; 100]
t_M [μm]	Thickness of Membrane	[1; 5; **10**; 50; 100; 500; 1000]
L_M [μm]	Length of Membrane	[0.1; 0.25; 0.5; 0.75; 1; 2.5; **5**; 7.5; 10; 25; 50; 75; 100]
H_{CC} [μm]	Height of Cell Channel	[10; 50; 100; **300***; 500; 1000; 5000; 10000]
H_{FC} [μm]	Height of Flow Channel	[10; 50; 100; **300***; 500; 1000; 5000; 10000]
Q_{in} [μl/h]	Inlet Flow Rate	[0.1 0.5 1 5 10 **50** 100 500 1000]
D [m^2/s]	Diffusion Coefficient Rate	[1×10^{-13}; 1×10^{-12}; 1×10^{-11}; 1×10^{-10}; 1×10^{-9}; **3.39×10^{-9}***;1×10^{-8}; 1×10^{-7}]

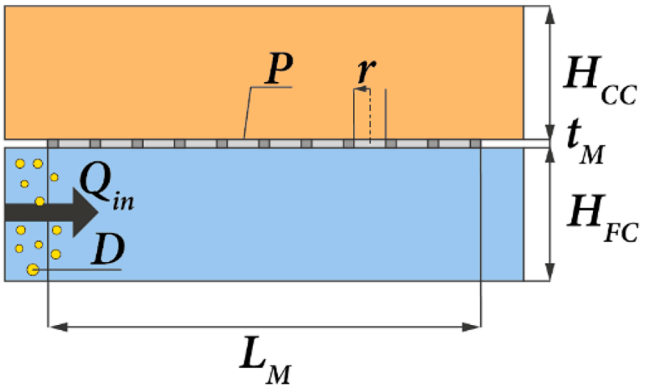

Fig. 2. . Illustration of the control parameters in analysis.

2.4. Variables of analysis

2.4.1. Fluidic field

Volumetric flow rate, Q [µl/h], is a crucial factor in many biological processes, such as accelerating phenotypic change of cells [69] or altering gene expression and biosynthesis of endothelial cells [70]. It is calculated as follows:

$$Q = v(H \bullet W) \tag{8}$$

Where H and W are respectively the height and width of the channel with media flow. Q was further normalised in relation to the inlet flow rate, $Q_n = Q/Q_{in}$, and analysed along the channels parallel to the direction of perfusion, in both the *CC* and the *FF*, respectively Q_{nCC} and Q_{nFC}, as illustrated in Fig. 4 a). Representing, perhaps, one of the most critical manifestations of fluid flow in biological applications [48], responsible for promoting vasculature growth in embryonic cardiovascular development [71], changing hepatocyte morphology and function [46,72] and even resulting in the direct destruction of cells [47], wall shear stress, *WSS* [Pa], was also analysed. By considering the media as being a Newtonian fluid, *WSS* was calculated as follows:

$$WSS = \gamma\mu \tag{9}$$

Where Υ represents the shear rate [s^{-1}]. *WSS* was analysed in data sets placed at cell height, defined as 10 µm [73], in the membrane surface of both the *FC* and *CC*, and in the upper surface of the *CC*, as illustrated in Fig. 4 b) and respectively identified as WSS_{MFC}, WSS_{MCC} and WSS_{UCC}.

Finally, the Reynolds number, *Re*, is an important dimensionless number for fluidic analysis. It is defined by the ratio between inertial and viscous forces, and it is commonly employed to determine the fluidic regime of a certain environment. It is defined as follows:

$$Re = \frac{\rho v D h}{\mu} \tag{10}$$

Where D_h represents the hydraulic diameter. Given the nature of microfluidics, *Re* is usually of very low magnitude, characterizing highly laminar systems [10,17]. For this reason, both *Q* and *WSS* were analysed for their steady response alone.

2.4.2. Mass transport

High resolution control over the delivery of soluble factors is a key advantage of OoaC technology [74]. Providing accurate biochemical cues, such as concentration gradients [75], continuous nutrient exchange, waste removal and hormonal flux [19], and delivery of soluble factors, such has growth factors and peptides [76], is critical for the establishment of relevant physiological environments. Therefore, data on molecular concentration, C, was normalized, C_n (=C_{in}/C), in relation to the inlet concentration, C_{in}, and measured as an average for both the *CC* and *FC*, identified respectively by C_{nCC} and C_{nFC}, as shown in Fig. 4 d).

Considering the time-dependency of molecular transport, highlighted by Equation 6), C_n was studied for both its transient and steady state behaviours. For the transient response, the time it takes for molecular transport to occur before stabilizing into a steady state, known as settling time, *st* [s], was analysed, as illustrated in Fig. 4 d), for both the *CC* and the *FC*, represented by st_{CC} and st_{FC} respectively. For the steady state, the normalized concentration at which molecular transport stabilizes, ssC_n, was also measured, as illustrated in Fig. 4 d). Measurements were done for both the *CC*, ssC_{nCC}, and the *FC*, ssC_{nFC}.

Finally, the Péclet Number, *Pe*, is a dimensionless number of great interest in the analysis of transport phenomena. It is defined by the ratio between advective and diffusive rates of transport, and can be expressed as follows:

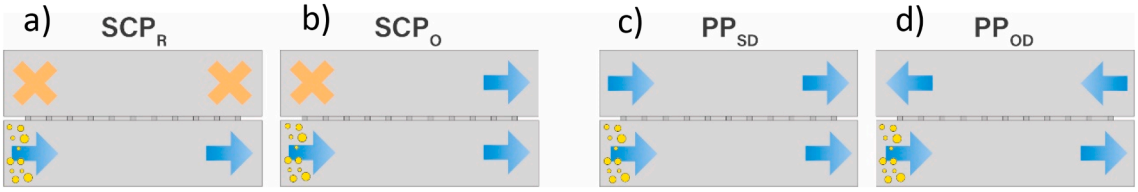

Fig. 3. . Schematic representation of the fluidic conditions tested, illustrating the boundary conditions for fluid flow and molecular transport, where in a) it is represented SCP_R, in b) SC_{PO}, in c) PP_{SD}, and in d) PP_{OD}.

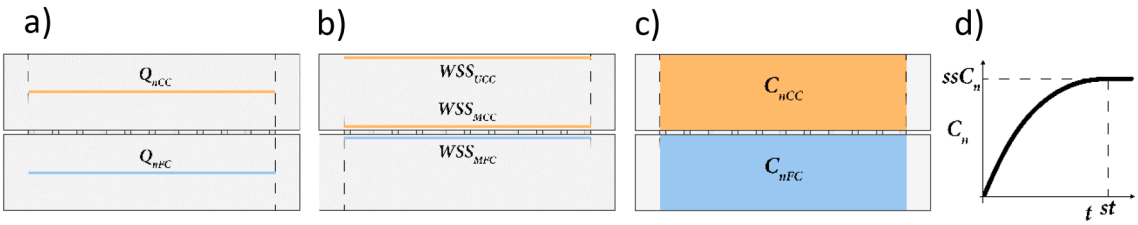

Fig. 4. . Location and geometry of data sets employed to measure, a), the normalized flow in both channels, respectively nQCC and nQFC, b), the shear in both the membrane surface of the FC, WSS_{MFC}, and the CC, WSS_{MCC}, and in the upper surface of the CC, WSS_{UCC}, and c) the transient and steady state molecular concentration distribution in the CC, CnCC, and the FC, CnFC. d) Illustration of a time-dependant concentration measurement, from which it is calculated both the steady state normalized concentration, ssC_n, and the settling time, st.

$$Pe = \frac{vDh}{D} \tag{10}$$

A system displaying $Pe > 1$, is characterized by the dominant influence of advection, as the main mode of transport. In turn, $Pe < 1$ characterizes diffusion as being the predominant transport phenomena.

2.5. Model validation

Towards verifying the predicative capabilities of the developed model, two distinct literature experiments were replicated, each aiming to address a different component of simulation. Therefore, the works of Chen et al 2020 [50] and Frost et al 2019 [54] were simulated towards verifying the model's capability on predicting both the fluid field and molecular transport respectively.

The work of Chen et al 2020 [50] performed Immersed Boundary Methods (IBM) simulations towards characterizing the relationship between flow features and the design properties of a microfluidic bilayer device with an integrated membrane. Beyond many other experiments, the relationship of L_m with both Q_{in}, v_n and WSS_n were studied and plotted. The geometric structure and fluidic conditions of the respective experiment were simulated by the present model, and the obtained results can be observed by the continuous lines in Fig. 5 a), b) and c), for Q_{in}, v_n and WSS_n respectively, superimposed over the original data, identified with markers or dashed lines. It can be analysed that there is a very clear affinity between the data provided by the present model and that reported by Chen et al, where the relationship between L_m and the various response variables match accurately. More so, Fig. 5 d) demonstrates that the flow velocity profile, measured vertically along the channels for different values of L_m is also represented equally between both models.

Frost et al 2019 [54] researches the transient response of the molecular concentration distribution of a microfluidic bilayer device with an integrated membrane. From the data provided, both numerical and experimental, the relationship between Q_{in} and C_{nCC}, is here presented and simulated, as demonstrated in Fig. 5 e). Identified by the point markers, in triangles, squares and circles, it is the experimental data, whereas in dashed lines it is the exponential fitted function, both provided by Frost et al. This data is referred to the transport of fluorescein, $D = 5.4 \times 10^{-10}$ m^2/s through a membrane with $P = 0.1$. On the other hand, identified by the continuous lines, it is the numerical data provided by the present model. It is possible to observe that, for all three tested Q_{in}, the C_n distribution follows a very similar trend, characterized by a steeper initial increase, later settling into a steady state and fixed value. Despite some differences between the shape of the exponential fit, as described by Frost et al, and the numerical data, provided by the present model, the latter presents, nonetheless, a great affinity with the experimental results, always remaining within the standard deviation intervals provided. Furthermore, it is also seen that the steady state values, for all three functions, also present a good match between experimental, exponential fit and numerical. The highest deviation was found for the condition of $Q = 100$ μL/h (Fig. 5 e), black line) and equivalent to a difference of $C_{nCC} = 0.02$.

3. Results and discussion

3.1. Fluidic field

3.1.1. Single channel versus parallel perfusion

The boundary conditions defining *SCP* imply that flow in the *CC* is always a function of both the properties of the membrane and Q_{FC}. Fig. 6 demonstrates that, if for SCP_R (Fig. 6 a)), the *CC* experiences a pressure similar to the outlet, in this case 0 Pa, for SCP_O (Fig. 6 b)), the pressure will be equivalent to the average value of the gradient established in the *FC*. It results that the *CC* experiences peak volumetric flow halfway the length of the membrane for SCP_R, as demonstrated in Fig. 6 c), and a continuously growing flow for SCP_O, as shown in Fig. 6 d). More importantly though, Fig. 6 c) and d) demonstrate respectively for SCP_R and SCP_O, how heavily dependent flow in the *CC* is on passive parameters, such as the *P*.

On the other hand, the boundary conditions characterizing *PP* imply that both channels are perfused with independent perfusion of media. For PP_{SD}, a null pressure gradient is defined between the *CC* and *FC* due to their equal pressure profiles, as shown in Fig. 7 a). In the absence of a driving pressure potential, media is hindered from crossing the membrane, resulting in a constant fluidic profile along the channels. This balance is strongly imposed by the perfused media, meaning that changes to passive parameters, such as *P*, will often play negligible effects in the fluidic microenvironment, as Fig. 7 c) demonstrates. For PP_{OD}, however, the symmetry between the pressure gradients of both the *CC* and *FC*, demonstrated in Fig. 7 b), promotes a small exchange of media across the membrane. Ultimately, a faint curvature of the fluidic profile is generated. This exchange means the fluidic profile in both channels is significantly more dependent on the membrane properties,

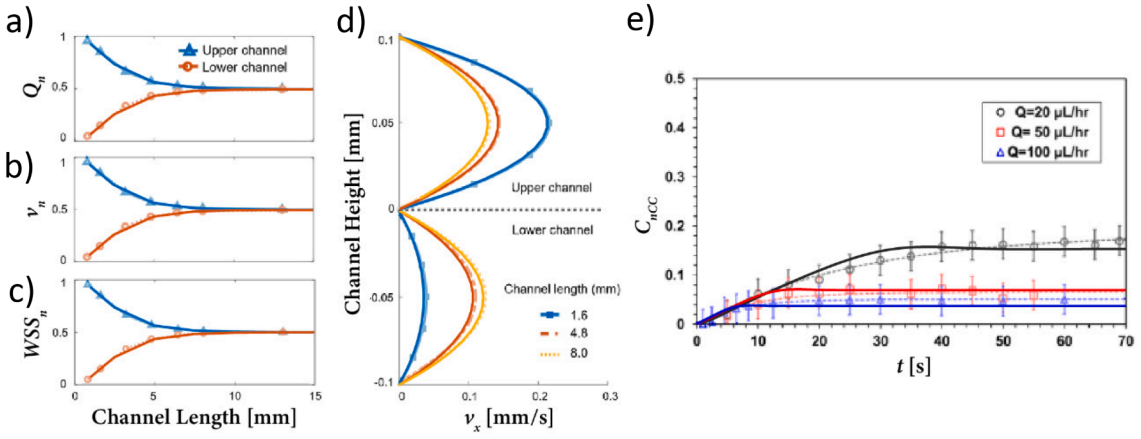

Fig. 5. . The various experiments replicated with the present model to verify its capability in predicting both the fluidic field and molecular transport. The results provided by Chen et al 2020 on simulating Q_n, in a), v_n, in b), WSS_n, in c), and v_x, in d), identified in either dashed lines or with markers, were successfully replicated by the current model, whose results are presented superimposed, in continuous lines. In e), the experimental data provided by Frost et al 2019 is identified by coloured markers, characterizing the transient concentration of fluorescein for a membrane with P = 0.1 and different Q, and in dashed lines, the respective exponential fit. Overlapping the respective results, it is presented the data simulated by the present model, identified by the continuous lines.

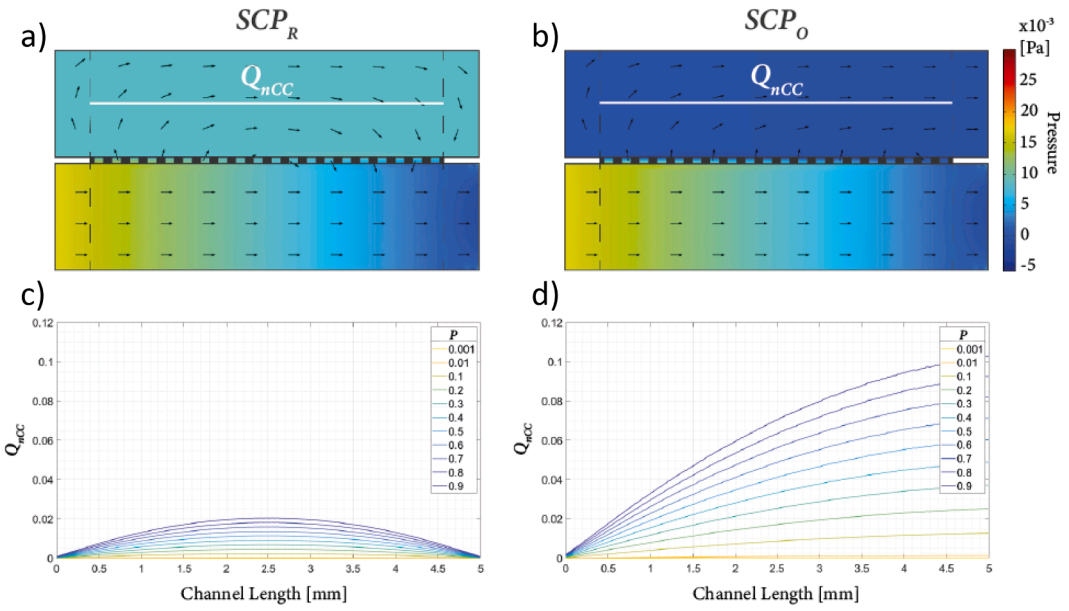

Fig. 6. . Characteristic pressure distribution, a) and b), and fluidic profile, c) and d), of the two distinct SCP conditions tested, SCP_R, in a) and c), and SCP_O, in b) and d). In a) and b), beyond the pressure distribution, it is also demonstrated the resulting fluidic field, identified by the black arrows. In c) and d), the fluidic profile for the CC is measured for different values of P, demonstrating the influence of the respective parameter in controlling Q_{nCC} for SCP.

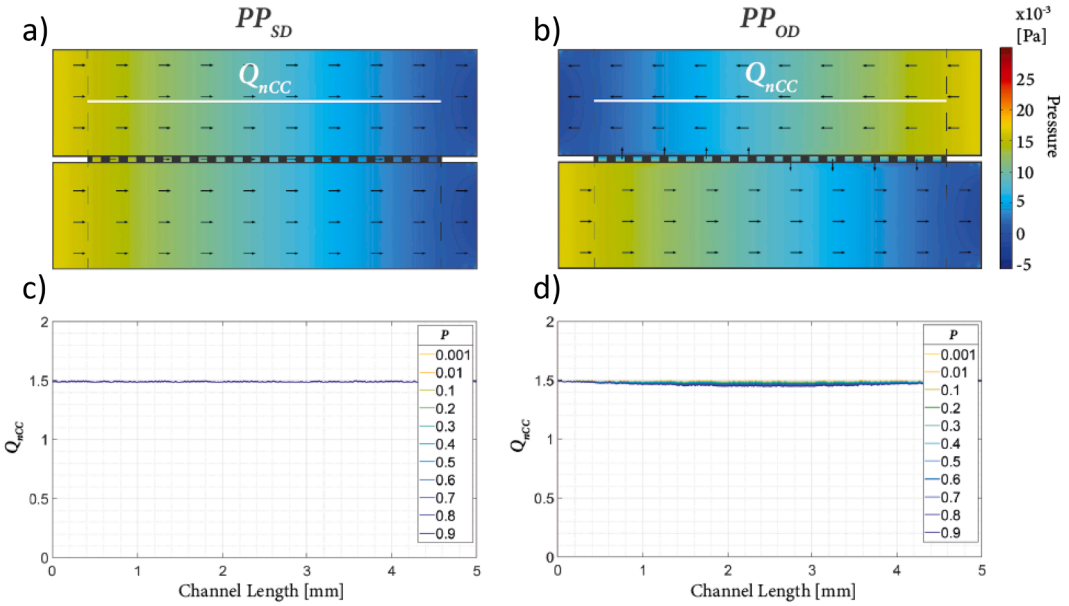

Fig. 7. . Characteristic pressure distribution, a) and b), and fluidic profile, c) and d), of the two distinct PP conditions tested, respectively PP_{SD}, in a) and c), and PP_{OD}, in b) and d). In a) and b), beyond the pressure distribution, it is also demonstrated the resulting fluidic field, identified by the black arrows. In c) and d), the fluidic profile of the CC is measured for different values of P, demonstrating the influence of the respective parameter in controlling Q_{nCC} for PP.

as demonstrated in Fig. 7 d) for the case of *P*.

Here on, Q_n and *WSS* will be studied as a direct function of control parameters, by analysing their average value, Q_n^A and WSS^A, along the respective data sets. The analysis will primarily focus on SCP_R, where results were found to be more meaningful. Otherwise, the reader is referred to Fig. A.1 and SM A.1, where the results and discussion for all conditions are present. Finally, an analysis to the Reynolds number is included in Table A.1. It is possible to, first, verify the highly laminar nature of flow, generally with $Re \ll 1$, and second, the differences between *SCP* and *PP*, where *Re* in the *CC* is significantly larger for the latter due to the independent perfusion.

Box 1

Design guidelines for modelling fluid dynamics with different fluidic setups.

- **Single Channel Perfusion, *SCP*:** Extremely relevant for modelling flow in the *CC* with passive parameters. A change from SCP_R to SCP_O increases fluidic exchange and flow in the *CC*.
- **Parallel Perfusion, *PP*:** Firmly governed by the imposed Qin and generally unaffected by changes in passive parameters. The symmetric pressure gradients in *PP* provide a slight increase to fluidic exchange.

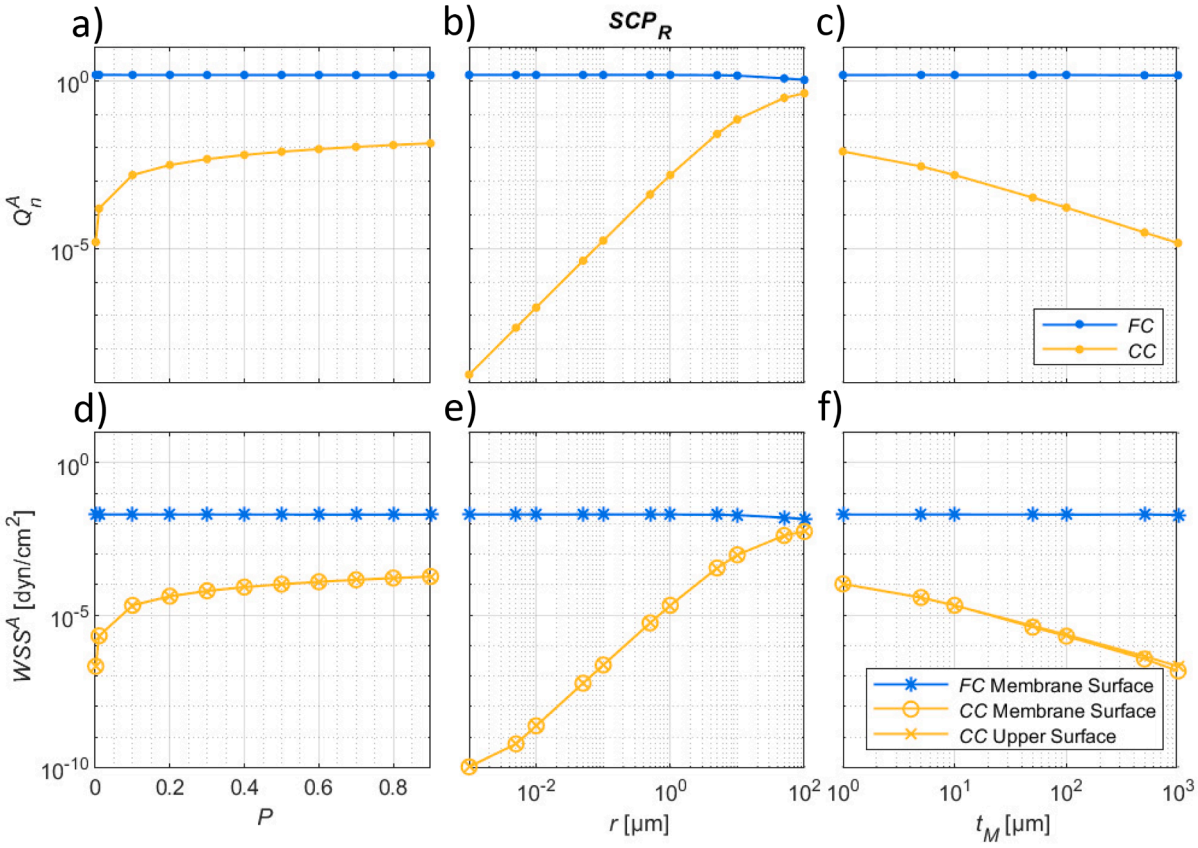

Fig. 8. . Membrane properties and their respective effect in modelling both the Q_n^A and WSS^A for SCP_R.

3.1.2. Membrane properties

The effects of P on the Q_n^A and WSS^A are presented in Fig. 8 a) and d) respectively. It is observed, through the yellow-dotted line, that for a $P < 0.2$, Q_{nCC}^A will experience an exponential decrease, reaching a value on the order of -5 for $P = 0.01$ (Q_{nCC}^A ($P = 0.01$) $= 1.55 \times 10^{-5}$, Table A.1), corresponding to a 2.5-fold reduction. On the other hand, for $P > 0.2$, it is observed that the function gradually levels out, where Q_{nCC}^A increases by a mere 0.5-fold until $P = 0.9$. The correlations are similar for WSS, as shown in Fig. 8 d). It is analysed that higher control over WSS_{CC}^A is obtained for $P < 0.2$, where an exponential decrease leads to a value on the order of -7 dyn/cm^2 for a $P = 0.01$ (WSS_{CC}^A ($P = 0.01$) $= 2.10 \times 10^{-7}$ dyn/cm^2, Table A.1). Given the nature of SCP_R, the changes of WSS_{FC}^A in relation to P are negligible, regarding both Q_n^A and WSS^A.

Changing r presents a more linear response within the CC, as seen in yellow in Fig. 8 b) and e), for Q_{nCC}^A and WSS_{CC}^A respectively. This change, however, is of much greater magnitude. It is seen that, if for nanopores, with $r = 0.001$ μm, Q_{nCC}^A has an order of magnitude of -9 (Q_{nCC}^A ($r = 0.001$) $= 1.73 \times 10^{-9}$, Table A.1), this value increases to the order of 0 for an $r = 100$ μm (Q_{nCC}^A ($r = 100$) $= 0.42$, Table A.1), almost reaching a balance with the Q_{nFC}^A. A similar relationship is observed for WSS^A, where the usage of nanopores results in virtually shear-free environment, with WSS^A on the order of -10 dyn/cm^2 (WSS_{CC}^A ($r = 0.001$) $= 1.06 \times 10^{-10}$dyn/cm^2, Table A.1). Aside for values of r superior to 10 μm, where both the Q_n^A and WSS^A demonstrate a very gentle decrease, the flow dynamics in the FC suffers virtually no changes.

An increase of t_M will enhance pore resistance and hinder porous flow, which justifies the inversely proportional relationship with Q_{nCC}^A and WSS_{CC}^A seen in Fig. 8 c) and f) with the yellow-dotted lines. It can be analysed that, for $t_M = 1$ μm, Q_{nCC}^A is on the order of -2 and WSS_{CC}^A of -4 dyn/cm^2 (Q_{nCC}^A ($t_M = 1$) $= 7.80 \times 10^{-3}$ and WSS_{CC}^A ($t_M = 1$) $= 1.06 \times 10^{-4}$ dyn/cm^2, Table A.1). On the other hand, increasing t_M to 1000 μm will result on a decrease of Q_{nCC}^A and WSS_{CC}^A by approximately 3-fold (Q_{nCC}^A ($t_M = 1000$) $= 1.45 \times 10^{-5}$ and WSS_{CC}^A ($t_M = 1000$) $= 1.48 \times 10^{-7}$ dyn/cm^2, Table A.1). Finally, the blue lines in Fig. 8 c) and f) demonstrate that Q_{nFC}^A and WSS_{FC}^A experience virtually no change with t_M.

Box 2

Design guidelines for modelling fluid dynamics in *SCP* using membrane parameters.

- **Porosity, *P*:** Especially influential for values below 0.2, where both Q_{nCC}^A and WSS_{CC}^A present an exponential decrease.
- **Pore Radius, *r*:** Extremely relevant in controlling both Q_{nCC}^A and WSS_{CC}^A, being able to define virtually shear-free microenvironments for nanopores.
- **Membrane Thickness, t_M:** Provides a moderate, linear, inversely proportional relationship with both Q_{nCC}^A and WSS_{CC}^A.

3.1.3. Channel geometry

By controlling the surface area available for fluidic exchange, a change of L_M will correspond to a linear variation of Q_{nCC}^A, as visible in the yellow-dotted line of Fig. 9 a). For the interval tested, delimited by $L_M = 0.1$ mm and $L_M = 100$ mm, Q_{nCC}^A increased from a magnitude of -6.3 to -0.5, nearly reaching a balance with Q_{nFC}^A. A similar profile characterizes WSS_{CC}^A, as it is possible to observe in Fig. 9 c). At $L_M = 100$ mm, it was recorded maximum WSS_{CC}^A, with a value on the order of -2.3 dyn/cm^2 (WSS_{CC}^A ($L_M = 100$) $= 4.23 \times 10^{-3}$ dyn/cm^2, Table A.1). However, for smaller membranes, Fig. 9 c) highlights a critical length, at $L_M = 1$ mm, where the shear in the CC is experienced differently, depending on the surface of analysis. This feature can amount to a difference of 1.7 dyn/cm^2 orders of magnitude, for $L_M = 0.1$ mm, where $WSS_{MCC} > WSS_{UCC}$.

H_{CC} is directly responsible for controlling the cross-sectional area of the CC and hence, the Q_{CC}. The relationship displayed, however, as seen in Fig. 9 b), proves complex. For $H_{CC} = 10$ μm, Q_{nCC}^A is at its lowest, with

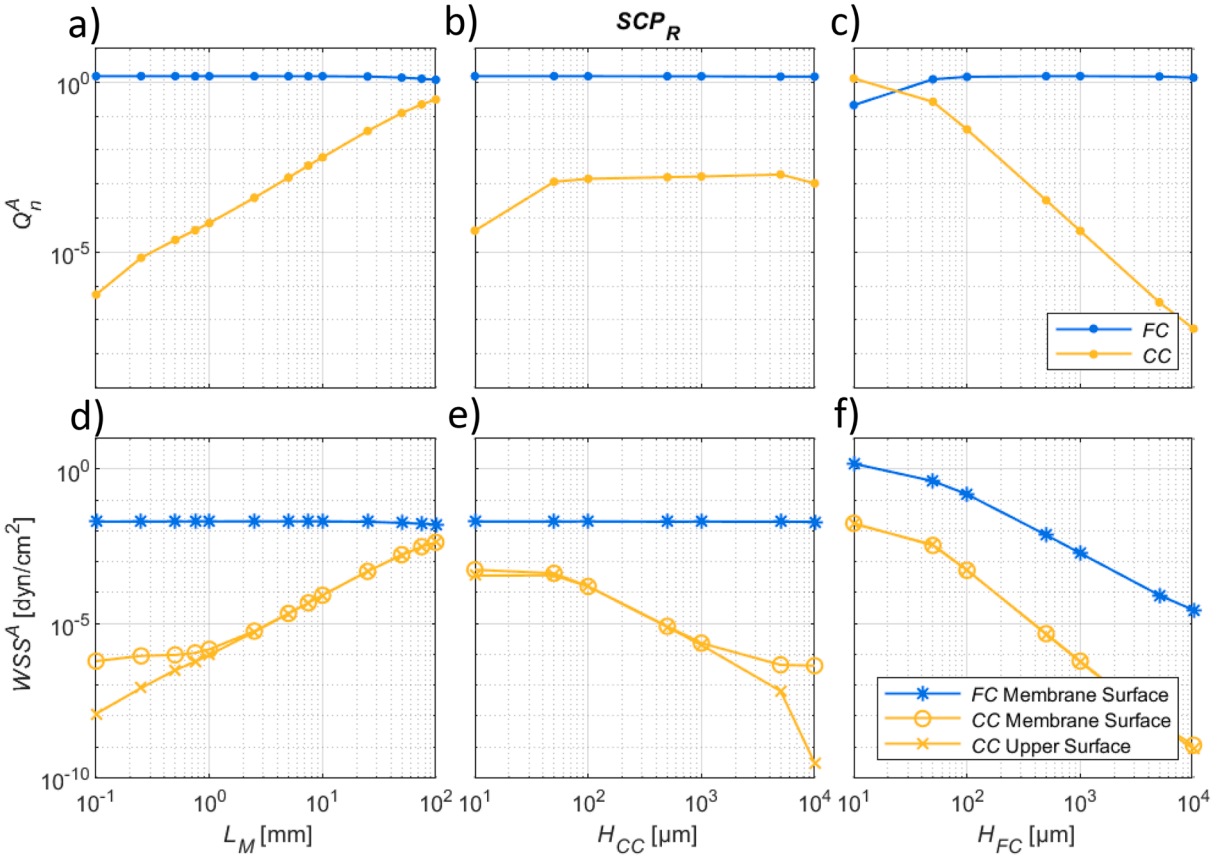

Fig. 9. . Channel geometry parameters and their respective effect in modelling both the Q_n^A and WSS^A for SCP_R.

a value on the order of −4.3 (Q^A_{nCC} ($H_{CC} = 10$) = 4.24×10^{-5}, Table A.1). Increasing the H_{CC} will, initially, also increase Q^A_{nCC}, until this value stabilizes in the order of −2.8. For $H_{CC} > 5000$ µm, however, it is observed that Q^A_{nCC} drops again, suggesting that the increase in chamber volume is no longer followed by a proportional increase of media exchange, ultimately decreasing Q^A_{nCC}. On the other hand, Fig. 9 e) demonstrates that an increase of H_{CC} corresponds to a continuous decrease of WSS^A_{CC}. And similar to L_M, it is observed that, for $H_{CC} > 1000$ µm, shear is experienced differently in the *CC*. The difference between WSS_{MCC} and WSS_{UCC} was measured to amount 3.2 dyn/cm^2 orders of magnitude, for $H_{CC} = 10{,}000$ µm.

The relationship between H_{FC} and Q, as seen in Fig. 9 c), demonstrates that, for shallower channels, with $H_{FC} = 10$ µm, high pressure will enhance media exchange across the membrane, ultimately determining $Q^A_{nCC} > Q^A_{nFC}$. By increasing H_{FC}, Q^A_{nFC} will similarly increase and stabilise above the inlet rate (Q^A_{nFC} ($H_{FC} = 100$) = 1.43, Table A.1). On the other hand, Q^A_{nCC} will continuously decrease, as low as −7.26 orders of magnitude for $H_{FC} = 10000$ µm (Q^A_{nFC} ($H_{FC} = 10{,}000$) = 5.53×10^{-8}, Table A.1). This reduction is equally felt on WSS^A_{CC}, where the latter variable drops from a magnitude of −1.8 dyn/cm^2, for $H_{FC} = 10$ µm, to −9.0, for $H_{FC} = 10{,}000$ µm. This decrease will also be accompanied by a decrease in WSS^A_{FC}, from the order of 0.17 dyn/cm^2, for $H_{FC} = 10$ µm, to −4.7, for $H_{FC} = 10{,}000$ µm.

Box 3

Design guidelines for modelling fluid dynamics in *SCP* using channel geometry.

- **Length of Membrane, L_M:** Linearly controls Q^A_{nCC} and WSS^A_{CC} and enables the differentiation of WSS^A_{MCC} and WSS^A_{UCC} for $L_M < 1$ mm.
- **Height of Cell Channel, H_{CC}:** Differentiates the magnitude of WSS^A_{MCC} and WSS^A_{UCC} for $H_{CC} > 1000$ µm.
- **Height of Flow Channel, H_{FC}:** Provides control over both WSS^A_{CC} and WSS^A_{FC} and uniquely enables $Q^A_{nCC} > Q^A_{nFC}$ for $H_{FC} \leq 10$ µm.

3.1.4. Flow and diffusion parameters

The analysis of Q^A was done in relation to its normalized values, Q^A_n, which justifies the horizontal functions seen in Fig. 10 a). However, it is worth noting that the ratio between Q^A_{nCC} and Q^A_{nFC} is unaffected by Q_{in}, given that both variables are kept at the same fixed values ($Q^A_{nCC} = 1.55 \times 10^{-3}$ and $Q^A_{nFC} = 1.49$, Table A.1). When it comes to WSS^A, Fig. 10 c) shows how increasing Q_{in} results in a likewise linear and proportionate increase of WSS^A in both channels. If in the *FC*, WSS^A ranges from a magnitude of −4.39 to −0.39 dyn/cm^2, for the studied interval of Q_{in}, in the *CC*, it ranges between −8.37 and −4.37 dyn/cm^2.

On the other hand, it comes naturally that the effects of D on the established fluidic field are null, as the respective feature concerns the properties of diluted molecules alone. This way, the functions obtained describing Q^A_n and WSS^A are steady and horizontal, as seen in Fig. 10 b) and d) respectively.

Box 4

Design guidelines for modelling fluid dynamics in *SCP* using flow and diffusion parameters.

- **Inlet Flow Rate, Q_{in}:** Widely controls Q^A_n without changing the ratio between Q^A_{nCC} and Q^A_{nFC}, a feature exclusive for membrane and geometry parameters.
- **Diffusion Coefficient Rate, D:** Being exclusively a property of the diluted molecule, it does not influence the established fluidic field.

3.2. Mass transport

3.2.1. Single channel versus parallel perfusion

Given the single inlet for molecular input in *SCP*, Fick's Law determines that the flux of molecules from the *FC* to the *CC* only stabilizes when the concentration gradient between domains is null. To satisfy this condition, a steady state is only reached when $C_n = 1$, for either SCP_R or SCP_O, as demonstrated by Fig. 12 a) and b) respectively. Fig. 12 c) and d)

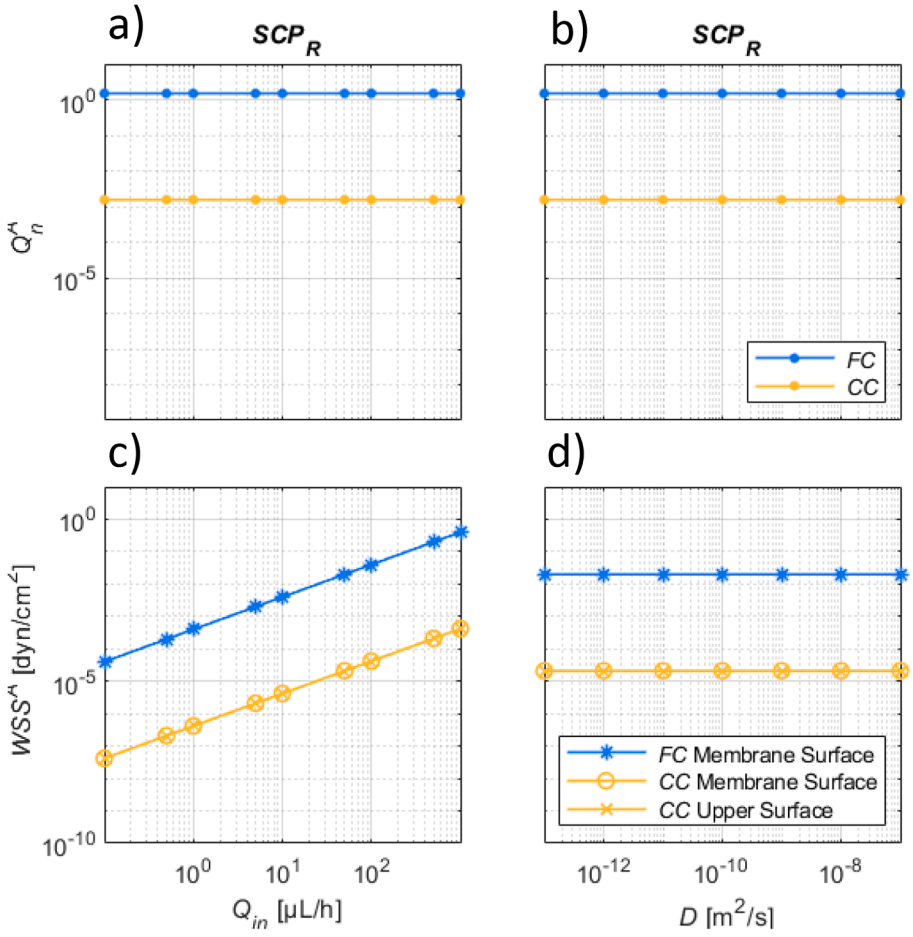

Fig. 10. . Flow and diffusion parameters and their respective effect in modelling both the Q_n^A and WSS^A for SCP_R.

further highlights that, regardless the size of the molecule, the tendency will always be to reach the normalized value of 1, and hence, equalizing C_{in}. The two fluidic conditions differ, however, in the role played by convection in defining molecular transport, where the increased porous flow in SCP_O enhances trans membrane transport. This phenomenon is especially noticeable for heavier molecules, with a lower D, whose higher reliance on convective transport results in greater kinetic changes between SCP_R and SCP_O, as evidenced in Fig. 12 c) and d) respectively.

On the other, in PP, the dual infusion of molecular concentration, with normalized inlet values of $C_{inFC} = 1$ and $C_{inCC} = 0$, Fick's Law determines that molecular transport will be done until a balance is reached between the *FC* and the *CC*. Therefore, the steady state balance in PP will

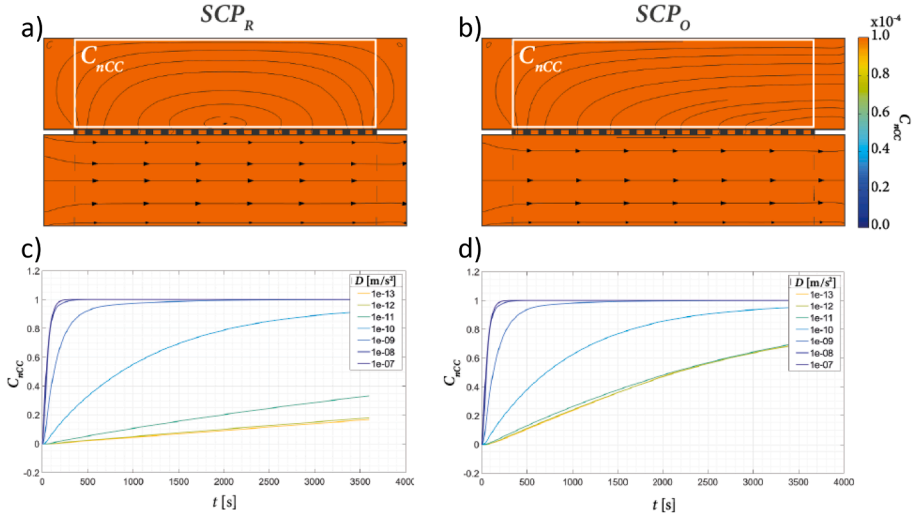

Fig. 11. . Characteristic steady state concentration distribution, a) and b), and transient molecular transport, c) and d), of the two distinct PP conditions tested, respectively PP_{SD}, in a) and c), and PP_{OD}, in b) and d). In a) and b), beyond the concentration distribution, it is also shown the molecular flux, identified by the black arrows. In c) and d), the transient molecular concentration of the CC is measured for different values of D.

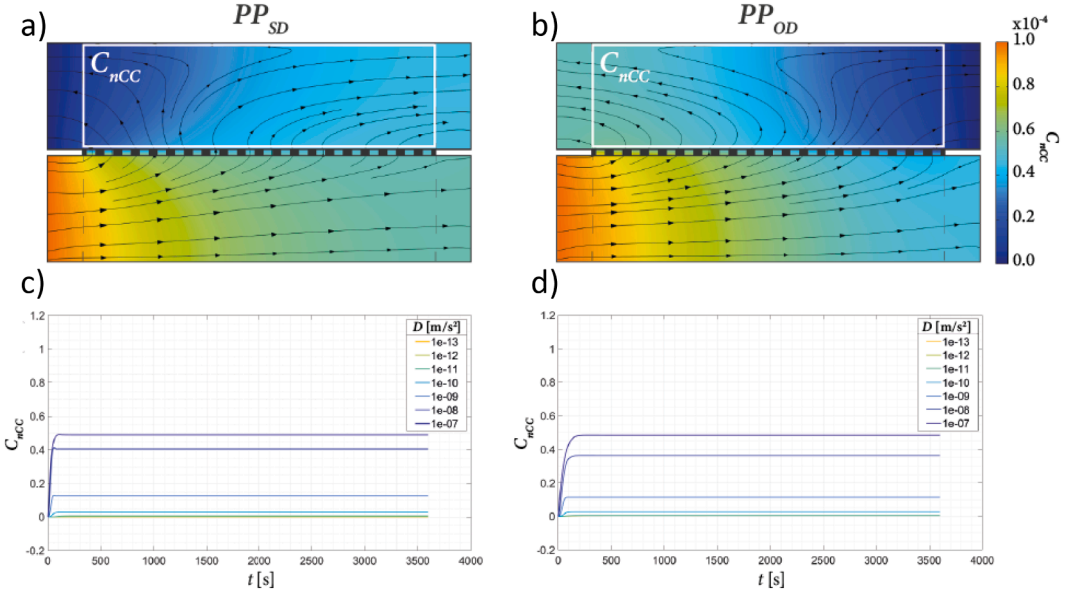

Fig. 12. . Characteristic steady state concentration distribution, a) and b), and transient molecular transport, c) and d), of the two distinct SCP conditions tested, respectively SCP_R, in a) and c), and SCF_O, in b) and d). In a) and b), beyond the concentration distribution, it is also shown the molecular flux, identified by the black arrows. In c) and d), the transient molecular concentration of the CC is measured for different values of D.

be heterogenous, as shown by Fig. 11 a) and b). The transient permeability curves of Fig. 11 c) and d) further highlight that the steady state is achieved for an intermediate concentration, whose value is dependent on the selected parameters and generally satisfies the condition $ssC_{nCC} + ssC_{nFC} = 1$. The differences between PP_{SD} and PP_{OD} are also highlighted, where the polarity of the concentration distributions follows each of the distinctive convective patterns, as seen in Fig. 11 a) and b) respectively. Further, despite evidencing short transient reactions, it is visible that PP_{SD} benefits molecular transport, resulting in faster transport and higher concentration ratios, as shown in Fig. 11 d), per comparison with c), for PP_{OD}.

Given that for *PP*, *st* is relatively low and often unresponsive to parametric changes, and that for *SCP*, ssC_n is always equal to 1, here forwards, the analysis will primarily focus on studying *st* for SCP_R, and ssC_n for PP_{SD}, with both as a direct function of control parameters. Nonetheless, the reader is referred to Fig. A.1 and SM A.1, where all results and respective discussion can be found. Finally, an analysis of the Péclet number is included in Table A.1. In general, it is observed that for *SCP*, transport in the *CC* is more subject to variations induced by a different choice of parameters, with Pe_{CC} fluctuating above and below the value of 1. On the other hand, it is observed that Pe_{CC}, for *PP*, and Pe_{FC}, for both *SCP* and *PP*, are generally maintained above the value of 1, suggesting that advection is the predominant mode of transport.

Box 5

Design guidelines for modelling molecular transport with different fluidic setups.

- **Single Channel Perfusion, *SCP*:** Determines a uniform concentration distribution equal to the inlet value, regardless of the selected passive parameters, but provides wide control over the rate of transient transport. The increase of convective flow in SCP_O provides slightly faster transport over SCP_R.
- **Parallel Perfusion, *PP*:** Capable of widely modelling the steady state concentration distribution based on the selected passive parameters. PP_{SD} provides a slight increase to the exchange rate, and therefore, decrease to *st*, when compared to PP_{OD}.

3.2.2. Membrane properties

The changes induced by a variation of *P* in SCP_R to *st* are present Fig. 13 a) and demonstrate the existence of a critical value at $P = 0.1$. For $P < 0.1$, it is observed that not only does st_{FC} decrease from $st_{FC} = 155$ s to $st_{FC} = 50$ s, for $P = 0.01$, but also, and more significantly, st_{CC} sharply increases, from $st_{CC} = 285$ s to $st_{CC} > 3600$ s. On the other hand, for $P > 0.1$, both functions stabilize and settle on the values of $st_{FC} = 135$ s and $st_{CC} = 185$ s. Similarly, Fig. 13 b) demonstrates that the correlation between *P* and ssC_n in PP_{SD} is also characterized by a critical value, this time at $P = 0.2$. For $P < 0.2$, the functions for ssC_{nCC} and ssC_{nFC} symmetrically, and respectively, decrease and increase, with a magnitude of approximately $ssC_n = 0.32$. For $P > 0.2$, both functions stabilize at the respective values of $ssC_{nCC} = 0.36$ s and $ssC_{nFC} = 0.64$ s.

Data for *r*, on the other hand, demonstrates a very passive behaviour. Fig. 13 a) shows that *st*, in *SCP*, is maintained stable for a wide range of *r*. Only for $r > 10$ μm it is possible to marginally reduce *st*, ultimately achieving $st_{CC} = 1755$ s and $st_{FC} = 95$ s for $r = 100$ μm. Regarding its parametric influence over ssC_n in *PP*, Fig. 13 e) demonstrates an even more passive relationship, where ssC_n remains virtually unaffected to any change in *r*.

The relationship between t_M and *st* in SCP_R is shown by Fig. 13 c). It is observed, with an increase of t_M, st_{CC} too widely increases, from the value of $st_{CC} = 190$ s, for $t_M = 1$ μm, to $st_{CC} > 3600$ s, for $t_M = 1000$ μm, Regarding st_{FC}, however, a much steadier profile is observed, maintaining within $st_{FC} = 135 - 150$ s for the majority of the values tested, but decreasing to $st_{FC} = 55$ s when $t_M < 500$ μm. On the other hand, Fig. 13 f) demonstrates that t_M produces a gradual change over ssC_n in PP_{SD}. Values for ssC_n steadily increase and decrease, in the *FC* and.

CC respectively, with an increase of t_M. It was analysed that an increase from $t_M = 1$ μm to $t_M = 1000$ μm will correspond to an absolute change equivalent to $ssC_n = 0.34$.

Box 6

Design guidelines for transient transport in *SCP* and molecular concentration in *PP* using membrane parameters.

- **Porosity, *P*:** For $P < 0.1$ and $P < 0.2$ it is possible to widely control *st* and ssC_n respectively.
- **Pore Radius, *r*:** Provides very modest control over *st*, for $r > 10$ μm, but no measured influence over ssC_n.
- **Membrane Thickness, t_M:** Increasing t_M provides a steep increase to st_{CC} and reduce membrane transport, characterized by an increase of ssC_{nFC} and decrease of ssC_{nCC}.

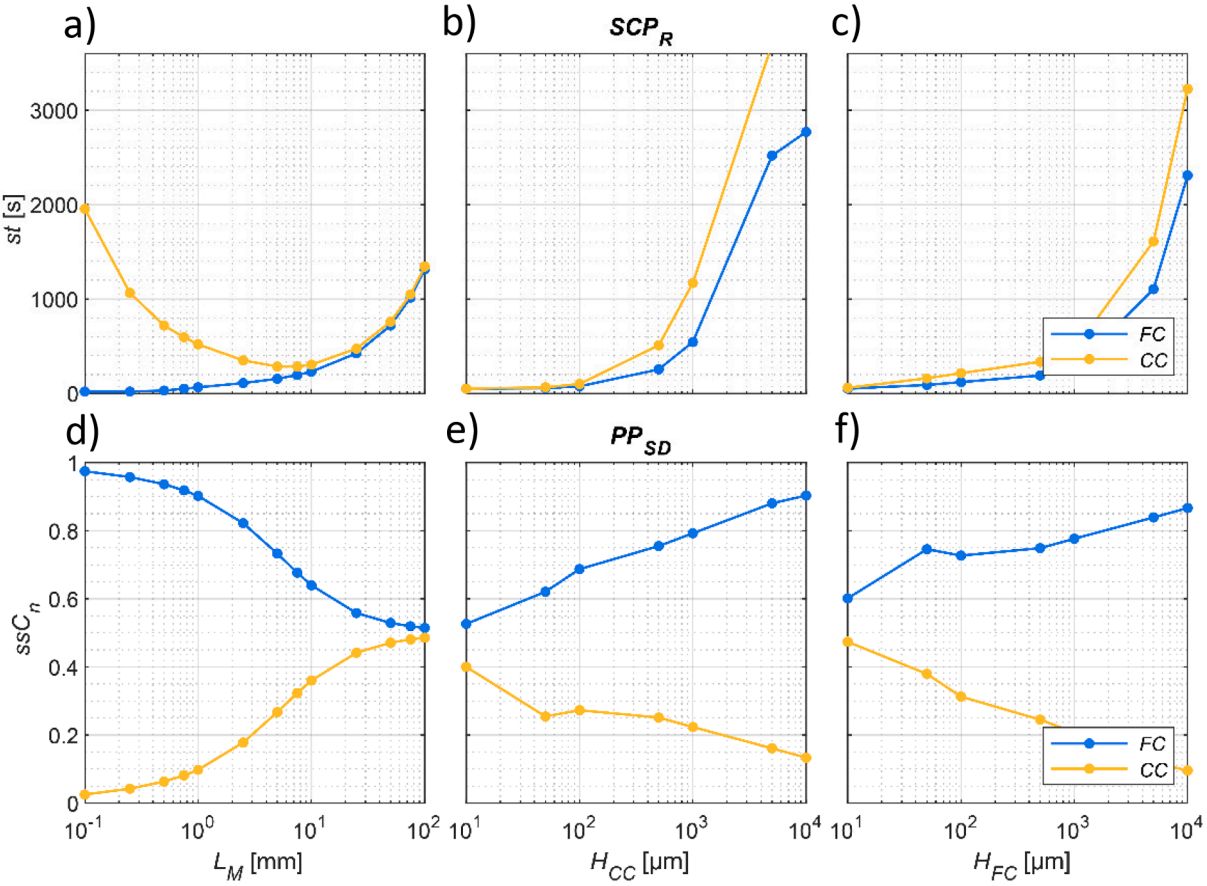

Fig. 13. . Channel geometry parameters and their respective effect in modelling both the st and ssC_n for SCP_R and PP respectively.

3.2.3. Channel geometry

A change in L_M affects both the surface area for porous exchange and the volume of channels. Each of these contributions will have a unique effect on molecular transport. Fig. 14 a), it is observed that st_{CC} in SCP_R is described by a quadratic function, with a lower limit at $st_{CC} = 285$ s, for $L_M = 5$ mm and $L_M = 7.5$ mm. For $L_M < 5$ mm, the decreasing exchange area will reduce molecular transport and increase st_{CC}. For $L_M > 7.5$ mm, the increasing exchange area is outweighed by the increasing volume of channels, ultimately increasing st_{CC}. For st_{FC}, Fig. 14 a) demonstrates that augmenting L_M will continually increase the latter variable. Regarding the influence of L_M in changing ssC_n in PP_{SD}, Fig. 14 d) demonstrates that an increase in L_M will likewise increase transport across the membrane, corresponding to $ssC_n = 0.46$. This means $ssCn_{CC}$ and $ssCn_{FC}$ very nearly reach a balance between channels.

Equivalent to a change of volume alone, increasing H_{CC} I will amount to a likewise increase of st in SCP_R, as Fig. 14 b) demonstrates. This increase is resembling an exponential where, if $H_{CC} = 10$ µm, $st_{CC} = st_{FC} = 50$ s, for $H_{CC} = 10000$ µm, $st_{CC} > 3600$ s and $st_{FC} = 2770$ s, indicating that a steady state will be reached generally faster in the *FC*. When it comes to ssC_n in PP_{SD}, the correlation is more resemblant of a inversely proportional linear function, where an increase to H_{CC} results in a decrease of molecular transport, as shown by Fig. 14 e). In turn, this defines a growing ssC_{nFC} and decreasing ssC_{nCC}.

Very similar relationships are observed for the changes induced by H_{FC} in both the st in SCP_R and the ssC_n in PP_{SD}, as Fig. 14 c) and f) respectively demonstrate. An increase of H_{FC} will correspond to an exponential increase of both st_{CC} and st_{FC}, even though generally, $st_{CC} > st_{FC}$. And regarding molecular transport if $H_{FC} = 10$ µm, $ssC_{nFC} = 0.60$ and $ssC_{nCC} = 0.47$, for $H_{CC} = 10000$ µm, $ssC_{nFC} = 0.87$ s and $ssC_{nCC} = 0.10$ s, evidencing a linear decrease followed by the increase of H_{FC}. H_{FC} and H_{CC} are the only cases where the condition $ssC_{nCC} + ssC_{nFC} = 1$ does not necessarily apply, due to the imposed geometric asymmetry.

Box 7

Design guidelines for transient transport in *SCP* and molecular concentration in *PP* using channel geometry.

- **Length of Membrane, L_M:** Provides full control over ssC_n and a quadratic function modelling st_{CC}, with a lower limit at $st_{CC} = 285$ s, for $L_M = 5$ mm and $L_M = 7.5$ mm.
- **Height of Cell Channel, H_{CC}:** Exponential control over st and inversely linear over ssCn, while creating asymmetries between *CC* and *FC*, being the exception to $ssC_{nCC} + ssC_{nFC} = 1$.
- **Height of Flow Channel, H_{FC}:** Exponential control over st and inversely linear over ssC_n, while creating asymmetries between CC and FC, being the exception to $ssC_{nCC} + ssC_{nFC} = 1$.

3.2.4. Flow and diffusion parameters

The relationship between Q_{in} and st in SCP_R is displayed by Fig. 15 a). It can be observed that an increase of Q_{in} will promptly accelerate the rate of transport, and therefore, reduce st. If for $Q_{in} \leq 1$ µL/h, st_{CC} and st_{FC} will be superior to 3600 s, for $Q_{in} \geq 100$ µL/h, both will already be inferior to 300 s, evidencing a very steep reduction of the transient interval. Regarding the parameter's influence over ssC_n in PP_{SD}, it can be seen that the relationship will be opposite, where an increase of Q_{in} corresponds to a decrease of molecular transport. As Fig. 15 c) demonstrates, whereas for $Q_{in} = 0.1$ µL/h, $ssC_{nCC} = 0.49$ and $ssC_{nFC} = 0.51$, characterizing a concentration balance between the channels, for $Q_{in} = 1000$ µL/h, $ssC_{nCC} = 0.04$ and $ssC_{nFC} = 0.96$, defining, instead, a full

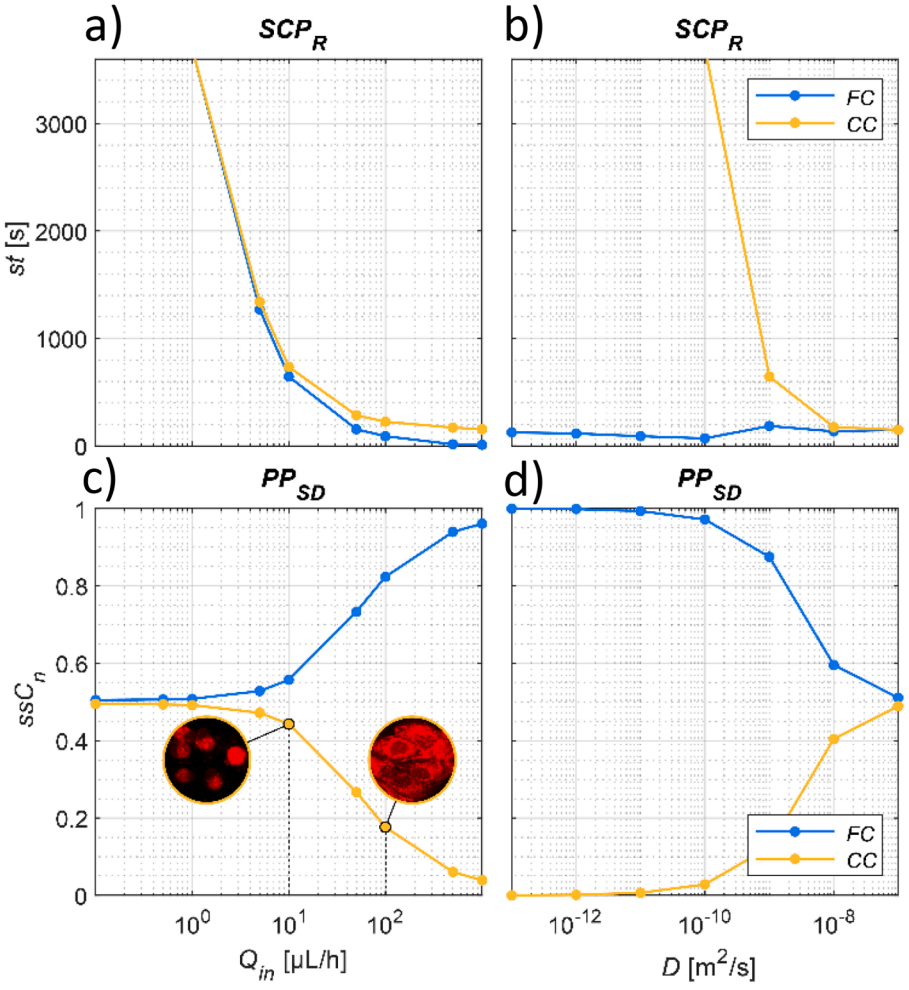

Fig. 14. . Flow and diffusion parameters and their respective effect in modelling both the st and ssC_n for SCP_R and PP respectively. In c), it is possible to observe that a decrease in Q_{in}, which results in an increase of the ssCnCC, will increase the transport of Cytochalasin D across the membrane, disrupting actin filaments and providing greater cell retraction. The respective experiment is described in further detail in the following.

contrast and evidencing very little signs of molecular exchange.

Box 8

Design guidelines for transient transport in *SCP* and molecular concentration in *PP* using flow and diffusion parameters.

- **Inlet Flow Rate, Q_{in}:** An increase to Q_{in} decreases molecular transport across the membrane but accelerates the exchange.
- **Diffusion Coefficient Rate, *D*:** An increase to *D* greatly decreases st_{CC}, without disrupting st_{FC}, and increases molecular transport across the membrane.

It comes naturally that a change in *D* will likewise impose changes in *st* in SCP_R and ssC_n in PP_{SD}, as seen in Fig. 15 b) and d) respectively. It can be observed that, a choice of a heavier molecule, will result in a long-reaching steady state in the *CC*, where for $D \leq 1 \times 10^{-10}$ m^2/s, $st_{CC} >$ 3600 s. On the contrary, a smaller molecule will travel faster through the membrane, and reach a steady state quicker. This way, for $D \geq 1 \times 10^{-8}$ m^2/s, $st_{CC} \leq 200$ s. More interestingly though, is that, regardless of the size of the molecule, st_{FC} remains rather steady, always kept within the interval between 70 and 185 s. This is justified by the role played by convection in the *FC*, which outweighs diffusion and outright defines the steady state. More obvious is the relationship between *D* and ssC_n in PP_{SD}, where an increase of *D* will equally correspond to an increase of molecular exchange, and therefore, we observe a decrease and increase of ssC_{nFC}.

3.3. Biological significance

To illustrate our numerical findings, we established a simple experimental setup which is illustrated by Fig. 16 a). It contains a platform with two separate microfluidic channels, separated by a porous membrane. Both channels are perfused with media, but only in one media is mixed with a given diluted molecule (channel in yellow, Fig. 16 a)). This way, we experimentally replicate PP_{SD}, where ssC_{nCC} is a function of the implemented control parameters. Two different membranes were tested, with a pore diameter of respectively 0.4 ($P = 0.01$) and 3.0 μm ($P = 0.17$). Similarly, to investigate Q_{in}, both membranes were tested at the flow rates of 10 and 100 μL/h. Initial experiments were performed with fluorescein (0.332 [KDa], 5.4×10^{-10} m^2/s), to describe permeability as a direct function of both *r* and Q_{in}. In parallel, Madin-Darby canine kidney (MDCK) cells were cultured *on-chip,* and their morphological behaviour studied as a function of the transport of Cytochalasin D across the membrane. The selection of fluorescein, as a fluorescent compound to study the permeability of the membrane, was done to obtain an approximation model for the transport of Cytochalasin D, given that both molecules have comparable molecular weight ($M_{\text{fluorescein}} = 332.3$ g/mol; $M_{\text{cytochalasin D}} = 507.6$ g/mol) and hence similar diffusion properties [77]. Both experiments provide experimental and biological evidence to support the present numerical data. Experimental details are

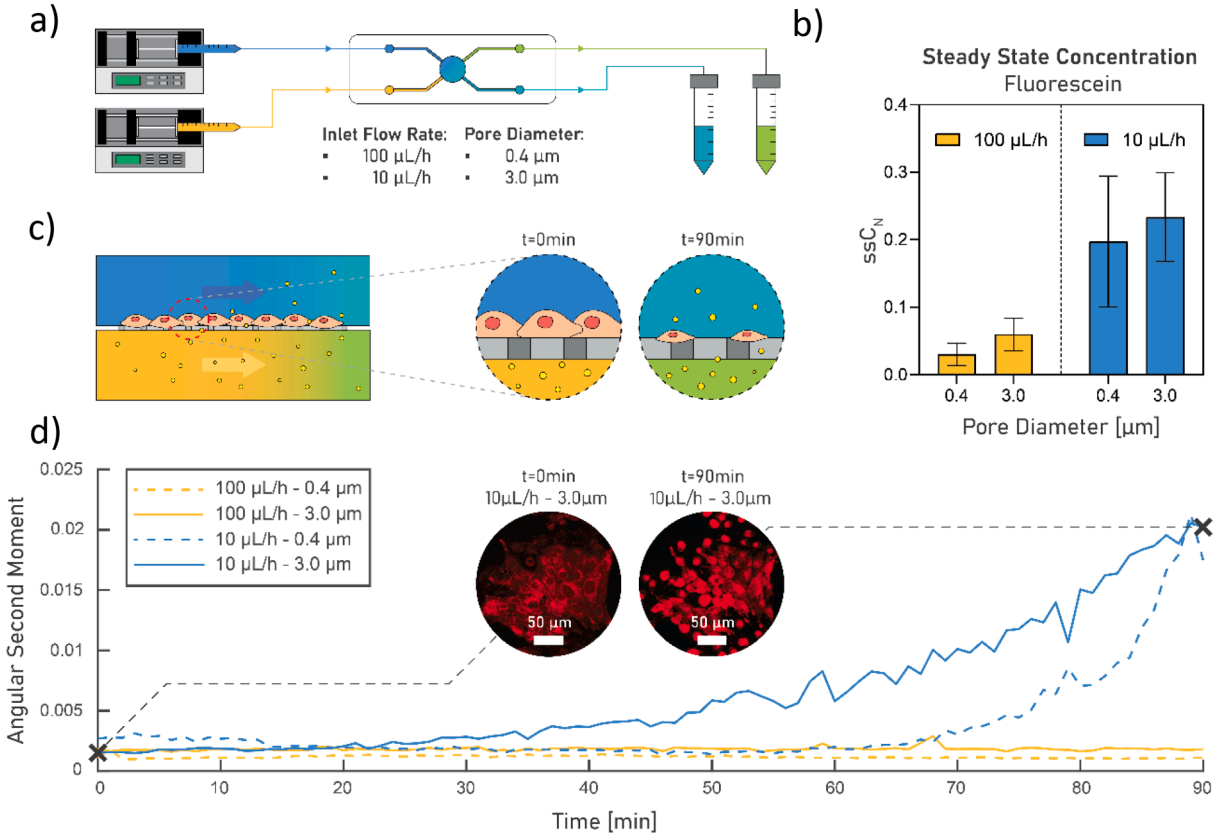

Fig. 15. . Schematic and results of on-chip experiments. In a), the experimental setup is illustrated, with fluidic pumps on the left, providing media with (in yellow) and without (in blue) a mixed diluted molecule to both channels of the microfluidic device in the middle, whose outlets are later connected to reservoirs, on the right. In b), a summary of the results obtained for the permeability of fluorescein at steady state are demonstrated, where in yellow the results at 100 µL/h are represented, and in blue those at 10 µL/h. In c), an illustration of the membrane chamber is illustrated, with cells sitting on the CC and evidencing the effect of the increasing concentration of Cytochalasin D along the duration of experiments. Finally, in d), the effect of Cytochalasin D is measured as a function of the angular second moment for the four conditions tested, with lines in yellow representing the conditions tested at 100 µL/h, in blue those at 10 µL/h, in continuous lines those performed with the 3.0 µm membrane, and in discontinuous lines with the 0.4 µm. Finally, fluorescent images with CellTracker Red CMTPX are also presented for the condition of 3.0 µm membrane at 10 µL/h, for the time frames of t = 0 min and t = 90 min. (For interpretation of the references to colour in this figure legend, the reader is referred to the web version of this article.)

found in the Supplementary Material.

The results for the permeability with fluorescein are present in Fig. 16 b), evidencing two key takeaways. First, that a change in membrane properties (pore diameter) produces very limited effect in controlling ssC_{nCC}, with a variance of only 0.03 when changing from r = 0.4 to 3.0 µm. And second, that Q_{in} provides dominant control over transport, displaying an increase of 0.17 in ssC_{nCC} when decreasing Q_{in} from 100 to 10 µL/h. Both results are in great conformity with those obtained numerically. As observed in Fig. 13 e), numerical data predicts a negligible influence of r in controlling transport, but it evidences, in d), a significant effect induced by the change in porosity. However, given the diffusion coefficient of fluorescein is lower than the one modelled (expressed in Table 1), Fig. 15 d) predicts that the diffusive component of transport will play a lesser role, and hence, membrane properties will provide a smaller influence in manipulating ssC_{nCC}, as observed experimentally. On the other hand, Fig. 15 c) verifies the dominant influence of Q_{in} in controlling ssC_{nCC}. Numerical data goes further in predicting an increase of approximately 0.26, when changing from Q_{in} = 100 to 10 [µL/h], a value which provides a good approximation to that obtained experimentally.

For the biological assays, chips were perfused with media (Gibco CO_2 independent media, Thermofisher) in both channels, and the *FC* supplied with Cytochalasin D at a fixed concentration of 20 µM. Using a confocal microscope (LSM800, Zeiss), the behaviour of the MDCK cells, cultured on the *CC*, was observed over a period of 90 min of perfusion and analysed as a function of the concentration of Cytochalasin D, transported from the *FC* to the *CC* via the porous membrane. Cytochalasin D is a well-known actin-disruptive toxin [78,79], whose inhibiting effect results in drastic changes in cell shape by reducing actin filament length. Its effect on MDCK is well-reported [80,81], and provides a good correlation to the concentration of the respective toxin in the surrounding microenvironment. Based on the respective measurement, *on-chip* experiments verified a similar trend to both numerical and fluorescent data, with conditions at lower Q_{in} contributing to a higher transport of Cytochalasin D across the membrane and into the *CC*, ultimately resulting in higher morphological change and greater cell retraction. In Fig. 16 d), the changes in cell morphology are quantified as a function of the angular second moment, a parameter which provides a measure of image homogeneity and can be used to detect morphological changes [82,83]. Plotting the respective parameter evidences a steeper −635224155increase for the conditions at 10 µL/h, as highlighted in blue, than for those at 100 µL/h, highlighted in yellow, which remain rather constant and horizontal. This is a manifestation of greater morphological change, and specifically, stronger cell retraction for the conditions at 10 µL/h then for those at 100 µL/h. This effect can be directly observed through the fluorescent images, taken by labelling MDCK cells with CellTracker Red CMTPX, present in Fig. 16 d) for the time frames of t = 0 min and t = 90 min, for the 3.0 µm membrane at 10 µL/h. On the other hand, the variation between membrane properties demonstrates, once again, a relatively passive role in controlling the

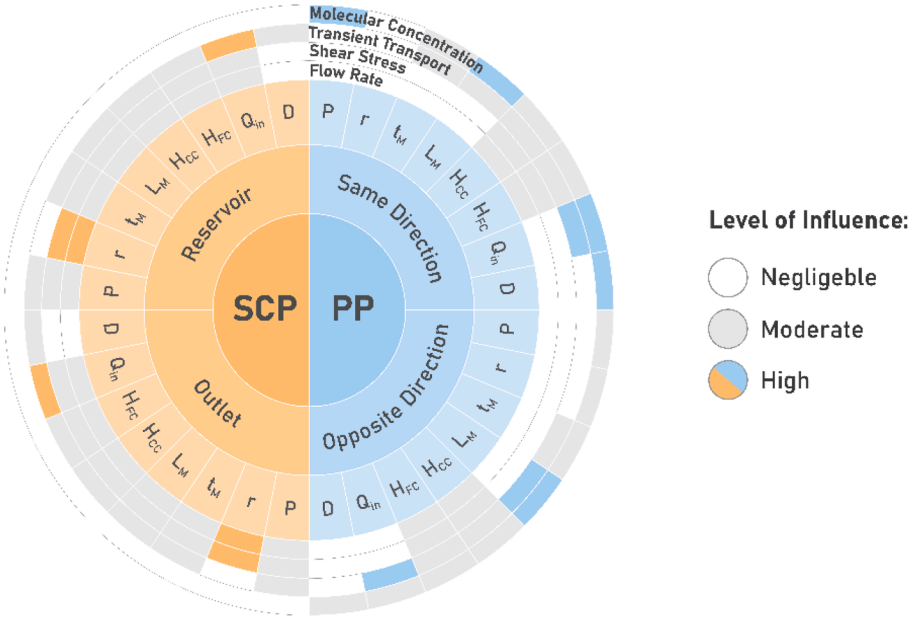

Fig. 16. . Summary of the results provided, with a hierarchical display of the influence played by setups and parameters on certain desired outputs. In green, it is highlighted the parameters with the best performances. (For interpretation of the references to colour in this figure legend, the reader is referred to the web version of this article.)

transport of molecules across the membrane. This is displayed in Fig. 16 d) by the small differences between the same-coloured curves, plotted with continuous and discontinuous lines for respectively the 3.0 and 0.4 μm membranes, manifesting minor morphological changes as a result of the different porous properties tested.

Crucially, both experiments demonstrate the biological impact of permeability mechanisms and, more importantly, the significance of the developed numerical guidelines in predicting the most relevant permeability parameters in regard to specific devices and biological applications.

4. Conclusion

A finite element model of a microfluidic bilayer device with integrated porous membrane has been established, providing extensive knowledge on the correlation between membrane integration parameters and resulting fluid dynamics and mass transport. The respective model enabled the development of a large-scale, systematic study, where eight distinct parameters, related to membrane, geometry, flow, and diffusion properties were individually researched. At the same time, four different fluidic conditions were, in parallel, tested, this way addressing a wider range of microfluidic architectures. All these parameters were then studied in relation to four distinct response variables, characterizing the steady state fluid flow, wall shear stress, and concentration distribution, as well as the transient convective-diffusive mass transport.

The obtained results provide a comprehensive analysis, with design guidelines for membrane integration in OoaC and microfluidic applications. The results are summarized below and complemented by Fig. 16 which highlights, in grey, the conditions providing significant influence over a certain desired output, and in orange and blue, those offering the most effective control.

- **Passive control over flow rate:** primarily relevant in *SCP*, with membrane properties and channel design parameters playing fundamental roles in modelling fluid flow in the *CC*. It is highlighted *r*, capable of modelling flow in the *CC* across 9 orders of magnitude, and H_{FC}, with the ability of reversing the flow ratio between channels. Otherwise, in *PP*, the flow dynamics are predominantly governed by Q_{in}, whose influence hinders the effects the remaining parameters potentially trigger.
- **Passive control over shear stress:** primarily relevant in *SCP*, where both membrane properties and channel geometry play crucial roles. More significantly, *r* is capable of modelling shear stress from high levels, for large pores, to virtually shear-free conditions, for nano pores, ranging a total of 7 orders of magnitude. The influence of L_M and H_{CC} is also of great interest, both capable of uniquely establishing different levels of shear on opposing surfaces of the same channel. On the other hand, in *PP*, *WSS* is primarily dominated by the influence of Q_{in}. The only exceptions are H_{CC} and H_{FC}, whose influence enables modelling the shear stress whilst keeping flow at a constant rate.
- **Passive control over transient transport:** significantly modelled by the majority of passive parameters across both *SCP* and *PP*. While *r* provided virtually no influence, a very sharp change was measured for $P < 0.1$. H_{CC}, H_{FC} and t_M demonstrated instead a more gradual control over the transient transport. On the other hand, L_M displayed a quadratic relationship in SCP, suggesting the existence of an optimal value for increasing the exchange rate, and provided better performance for PP_{OD} when compared with PP_{SD}. Finally, it was verified that an increase to Q_{in} widely contributes to increasing the exchange rate and reduce the transient interval.
- **Passive control over molecular concentration and distribution:** only possible in *PP*. Whereas for *SCP*, Fick's Law determines the molecular concentration distribution is necessarily equal to the inlet value, for *PP*, this balance can be modelled by the design parameters. Membrane properties, in particular *P*, for $P < 0.1$, and t_M, play influential roles. H_{CC} and H_{FC} evidence a linear correlation, and present a unique behaviour for PP_{OD}, with the ability of respectively saturating or depleting the microenvironment. The more significant contributions are, however, provided by L_M and Q_{in}, capable of modelling the concentration from a uniform distribution to an extreme heterogeneity between the channels, the *CC* and the *FC* becoming respectively depleted and saturated.

On-chip experiments were further carried out, providing fluorescent and biological evidence in support of the present numerical data. An experimental platform and protocol were developed to replicate PP_{SD} and analyse the transport of molecules across the membrane as a function of both membrane parameters, namely r and P, and flow properties, Q_{in}. Experiments with fluorescein evidenced a mainly convection-driven permeability, with Q_{in} displaying a dominant role over both r and P, whose control over ssC_{nCC} was limited. A similar trend was seen with the transport of Cytochalasin D, whose actin-disruptive effect, quantified by the angular second moment as a measure of cell retraction, manifested the dominant role of Q_{in} in controlling porous transport of Cytochalasin D and defining ssC_{nCC}. By verifying the same trends as numerically predicted, both experiments, fluorescent and biological, ultimately demonstrated the experimental significance of the provided numerical data.

As concluding reflection, it is crucial to realise the influence played by confluent tissue barriers in further shaping both the fluidic and mass transport dynamics within microfluidic bilayer devices with integrated porous membranes. By adopting an electrical circuit analogy, it is possible to defer that the permeability of a tissue barrier formed on a membrane, K, is the combined result of both the diffusive permeability of the tissue barrier, K_{tb}, and of the membrane, K_m [44]. The respective relationship can be expressed by the following expression:

$$\frac{1}{K} = \frac{1}{K_{tb}} + \frac{1}{K_m} \tag{12}$$

The implications of Equation 12 can be further appreciated through the work of Frost et al. 2019 [84], where the permeability of a microfluidic bilayer device was measured, using several different molecules, for a membrane with and without a confluent tissue barrier model. Not only does this work demonstrates the similarities between the permeability behaviours of each model, but also, the necessity of knowing the individual contributions of both the membrane and the tissue barrier. It highlights that, the design of a specific membrane platform, should contemplate the contributions of each, towards ensuring accurate biochemical outputs. Finally, membrane properties should also be considered regarding the cell behaviour and migration patterns they might induce and should be selected appropriately.

Finally, it is important to highlight the usage of hydrogel matrices which, combined with microfluidics, has generated wide interest. It is appreciated that, when it comes to replicating biological tissue constructs, the elasticity and 3D porous networks of hydrogels prove desirable for tissue emulation [85]. However, contrary to porous membranes, whose physics are extensively characterized and well established, hydrogel matrices can be notoriously unpredictable, due to their dynamic, irregular properties. Nonetheless, tortuosity models, and more noticeably, the Millington and Quark and Bruggeman models, have been growing as accurate models to predict hydrogel dynamics. Therefore, an effective diffusivity, such as the one described in Equation 7, can be calculated to describe the motion of a specific molecule more accurately within a certain hydrogel. Ultimately, it follows that the data here presented can be translated into hydrogels, by applying a tortuosity model and resulting diffusion factor.

CRediT authorship contribution statement

P.D. Menezes: Conceptualization, Methodology, Investigation, Visualization, Writing – review & editing. **S. Hecht:** Investigation, Formal analysis, Writing – review & editing. **A. Hunter:** Investigation. **N. Gadegaard:** Conceptualization, Methodology, Funding acquisition, Project administration, Resources, Supervision, Writing – review & editing.

Declaration of competing interest

The authors declare that they have no known competing financial interests or personal relationships that could have appeared to influence the work reported in this paper.

Data availability

Data will be made available on request.

Acknowledgements

This work was supported by the Research Council of Norway through its Centres of Excellence funding scheme, project number 262613. NG acknowledges funding from the Novo Nordisk Foundation Challenge Programme in Energy materials with biological applications (EMGUT): grant ref. No. NNF22OC0072961.

Appendix A. Supplementary data

Supplementary data to this article can be found online at https://doi.org/10.1016/j.cej.2023.148189.

References

[1] K. Ronaldson-Bouchard, G. Vunjak-Novakovic, Organs-on-a-Chip: a fast track for engineered human tissues in drug development, Cell Stem Cell 22 (3) (2018) 310–324.
[2] <Harrison et al. 1910.pdf>.
[3] D. Cook, et al., Lessons learned from the fate of AstraZeneca's drug pipeline: a five-dimensional framework, Nat. Rev. Drug Discov. 13 (6) (2014) 419–431.
[4] F. Pammolli, L. Magazzini, M. Riccaboni, The productivity crisis in pharmaceutical R&D, Nat. Rev. Drug Discov. 10 (6) (2011) 428–438.
[5] G.A. Van Norman, Limitations of animal studies for predicting toxicity in clinical trials: is it time to rethink our current approach? JACC Basic Transl. Sci. 4 (7) (2019) 845–854.
[6] P. Pound, Are animal models needed to discover, develop and test pharmaceutical drugs for humans in the 21st century? Animals (Basel) 10 (12) (2020).
[7] J.C. Madden, et al., A review of in silico tools as alternatives to animal testing: principles, resources and applications, Altern. Lab Anim. 48 (4) (2020) 146–172.
[8] J.A. Terrell, et al., From cells-on-a-chip to organs-on-a-chip: scaffolding materials for 3D cell culture in microfluidics, J. Mater. Chem. B 8 (31) (2020) 6667–6685.
[9] <Agenda2016#TopTenEmergingTechnologies.pdf>.
[10] N. Convery, N. Gadegaard, 30 years of microfluidics, Micro Nano Eng. 2 (2019) 76–91.
[11] M. Rahimnejad, et al., Engineered biomimetic membranes for organ-on-a-chip, ACS Biomater. Sci. Eng. 8 (12) (2022) 5038–5059.
[12] J.D. Caplin, et al., Microfluidic organ-on-a-chip technology for advancement of drug development and toxicology, Adv. Healthc. Mater. 4 (10) (2015) 1426–1450.
[13] S. Selimovic, M.R. Dokmeci, A. Khademhosseini, Organs-on-a-chip for drug discovery, Curr. Opin. Pharmacol. 13 (5) (2013) 829–833.
[14] B. Zhang, M. Radisic, Organ-on-a-chip devices advance to market, Lab Chip 17 (14) (2017) 2395–2420.
[15] N.T. Nguyen, et al., Design, fabrication and characterization of drug delivery systems based on lab-on-a-chip technology, Adv. Drug Deliv. Rev. 65 (11–12) (2013) 1403–1419.
[16] D.Z. Wang, et al., Organ-on-a-chip platforms for drug delivery and cell characterization: a review, Sensors Mater. 27 (2015).
[17] G.M. Whitesides, The origins and the future of microfluidics, Nature 442 (7101) (2006) 368–373.
[18] L.C. Delon, et al., A systematic investigation of the effect of the fluid shear stress on Caco-2 cells towards the optimization of epithelial organ-on-chip models, Biomaterials 225 (2019) 119521.
[19] S. Ahadian, et al., Organ-on-a-chip platforms: a convergence of advanced materials, cells, and microscale technologies, Adv Healthc Mater 7 (2) (2018).
[20] R.O. Rodrigues, et al., Organ-on-a-chip: a preclinical microfluidic platform for the progress of nanomedicine, Small 16 (51) (2020) e2003517.
[21] Sosa-Hernandez, J.E., et al., Organs-on-a-Chip Module: A Review from the Development and Applications Perspective. Micromachines (Basel), 2018. 9(10).
[22] Q. Wu, et al., Organ-on-a-chip: recent breakthroughs and future prospects, Biomed. Eng. Online 19 (1) (2020) 9.
[23] L. Tomlinson, et al., In vitro liver zonation of primary rat hepatocytes, Front. Bioeng. Biotechnol. 7 (2019) 17.
[24] F.T. Lee-Montiel, et al., Control of oxygen tension recapitulates zone-specific functions in human liver microphysiology systems, Exp. Biol. Med. (Maywood) 242 (16) (2017) 1617–1632.
[25] N.S. Bhise, et al., A liver-on-a-chip platform with bioprinted hepatic spheroids, Biofabrication 8 (1) (2016) 014101.

[26] B. Adibi-Motlagh, et al., *Immobilization of modular peptides on graphene cocktail for differentiation of human mesenchymal stem cells to hepatic-like cells*, Front. Chem. 10 (2022).
[27] A. Agarwal, et al., Microfluidic heart on a chip for higher throughput pharmacological studies, Lab Chip 13 (18) (2013) 3599–3608.
[28] N. Jalilinejad, et al., Electrically conductive carbon-based (bio)-nanomaterials for cardiac tissue engineering, Bioeng. Transl. Med. 8 (1) (2023) e10347.
[29] A. Benigni, M. Morigi, G. Remuzzi, Kidney regeneration, Lancet 375 (9722) (2010) 1310–1317.
[30] S. Yousaf, et al., Handbook of Tissue Engineering Scaffolds:, Volume Two, Elsevier Amsterdam, The Netherlands, 2019.
[31] O.Y.F. Henry, et al., Organs-on-chips with integrated electrodes for trans-epithelial electrical resistance (TEER) measurements of human epithelial barrier function, Lab Chip 17 (13) (2017) 2264–2271.
[32] H.J. Kim, et al., Human gut-on-a-chip inhabited by microbial flora that experiences intestinal peristalsis-like motions and flow, Lab Chip 12 (12) (2012) 2165–2174.
[33] G. Agrawal, A. Aung, S. Varghese, Skeletal muscle-on-a-chip: an in vitro model to evaluate tissue formation and injury, Lab Chip 17 (20) (2017) 3447–3461.
[34] S.H. Park, et al., Chip-based comparison of the osteogenesis of human bone marrow- and adipose tissue-derived mesenchymal stem cells under mechanical stimulation, PLoS One 7 (9) (2012) e46689.
[35] M.C. Liu, et al., Electrofluidic pressure sensor embedded microfluidic device: a study of endothelial cells under hydrostatic pressure and shear stress combinations, Lab Chip 13 (9) (2013) 1743–1753.
[36] M. Rahimnejad, et al., Prevascularized micro-/nano-sized spheroid/bead aggregates for vascular tissue engineering, Nano-Micro Letters 13 (1) (2021) 182.
[37] S.I. Ahn, Y. Kim, Human Blood-Brain Barrier on a Chip: Featuring Unique Multicellular Cooperation in Pathophysiology, Trends Biotechnol. 39 (8) (2021) 749–752.
[38] O. Akhavan, E. Ghaderi, Differentiation of human neural stem cells into neural networks on graphene nanogrids, J. Mater. Chem. B 1 (45) (2013) 6291–6301.
[39] K. Achberger, et al., Merging organoid and organ-on-a-chip technology to generate complex multi-layer tissue models in a human retina-on-a-chip platform, Elife 8 (2019).
[40] J.S. Lee, et al., Placenta-on-a-chip: a novel platform to study the biology of the human placenta, J. Matern. Fetal Neonatal Med. 29 (7) (2016) 1046–1054.
[41] M. Mastrangeli, et al., Organ-on-chip in development: Towards a roadmap for organs-on-chip, ALTEX 36 (4) (2019) 650–668.
[42] C. Ma, et al., Organ-on-a-Chip: A New Paradigm for Drug Development, Trends Pharmacol. Sci. 42 (2) (2021) 119–133.
[43] <Ching2021#OrganOnAChip#Review#AcademiaToIndustry#DrugDevelopment.pdf>.
[44] H.H. Chung, et al., Use of porous membranes in tissue barrier and co-culture models, Lab Chip 18 (12) (2018) 1671–1689.
[45] J.J. VanDersarl, A.M. Xu, N.A. Melosh, Rapid spatial and temporal controlled signal delivery over large cell culture areas, Lab Chip 11 (18) (2011) 3057–3063.
[46] Y. Tanaka, et al., Evaluation of effects of shear stress on hepatocytes by a microchip-based system, Meas. Sci. Technol. 17 (12) (2006) 3167–3170.
[47] T. Torii, M. Miyazawa, I. Koyama, Effect of continuous application of shear stress on liver tissue: continuous application of appropriate shear stress has advantage in protection of liver tissue, Transpl. Proc. 37 (10) (2005) 4575–4578.
[48] J.W. Song, et al., Computer-controlled microcirculatory support system for endothelial cell culture and shearing, Anal. Chem. 77 (13) (2005) 3993–3999.
[49] H.H. Chung, et al., Highly permeable silicon membranes for shear free chemotaxis and rapid cell labeling, Lab Chip 14 (14) (2014) 2456–2468.
[50] S. Chen, et al., Flow field analyses of a porous membrane-separated, double-layered microfluidic chip for cell co-culture, Acta Mech. Sin. 36 (3) (2020) 754–767.
[51] A. Tiraferri, et al., A method for the simultaneous determination of transport and structural parameters of forward osmosis membranes, J. Membr. Sci. 444 (2013) 523–538.
[52] T.Y. Cath, et al., Standard methodology for evaluating membrane performance in osmotically driven membrane processes, Desalination 312 (2013) 31–38.
[53] M.T. Rogers, et al., A high-throughput microfluidic bilayer co-culture platform to study endothelial-pericyte interactions, Sci. Rep. 11 (1) (2021) 12225.
[54] T.S. Frost, et al., Convection–diffusion molecular transport in a microfluidic bilayer device with a porous membrane, Microfluid. Nanofluid. 23 (10) (2019).
[55] M. Fakhraee, O. Akhavan, Ultrahigh permeable c2n-inspired graphene nanomesh membranes versus highly strained c2n for reverse osmosis desalination, J. Phys. Chem. B 123 (41) (2019) 8740–8752.
[56] M. Khosravikia, Quantitative model for predicting the electroosmotic flow in dual-pole nanochannels, Electrophoresis 44 (7–8) (2023) 733–743.
[57] A. Gillet, et al., Liposome surface charge influence on skin penetration behaviour, Int. J. Pharm. 411 (1) (2011) 223–231.
[58] O.A. Andreev, D.M. Engelman, Y.K. Reshetnyak, pH-sensitive membrane peptides (pHLIPs) as a novel class of delivery agents, Mol. Membr. Biol. 27 (7) (2010) 341–352.
[59] N.K. Inamdar, L.G. Griffith, J.T. Borenstein, Transport and shear in a microfluidic membrane bilayer device for cell culture, Biomicrofluidics 5 (2) (2011) 22213.
[60] M. Khosravikia, A. Rahbar-Kelishami, A simulation study of an applied approach to enhance drug recovery through electromembrane extraction, J. Mol. Liq. 358 (2022) 119210.
[61] S. Schneider, et al., Membrane integration into PDMS-free microfluidic platforms for organ-on-chip and analytical chemistry applications, Lab Chip 21 (10) (2021) 1866–1885.
[62] D. Huh, et al., Reconstituting organ-level lung functions on a chip, Science 328 (5986) (2010) 1662–1668.
[63] Y. Du, et al., Mimicking liver sinusoidal structures and functions using a 3D-configured microfluidic chip, Lab Chip 17 (5) (2017) 782–794.
[64] X. Yang, et al., Nanofiber membrane supported lung-on-a-chip microdevice for anti-cancer drug testing, Lab Chip 18 (3) (2018) 486–495.
[65] P. Loskill, et al., WAT-on-a-chip: a physiologically relevant microfluidic system incorporating white adipose tissue, Lab Chip 17 (9) (2017) 1645–1654.
[66] A. Carraro, et al., In vitro analysis of a hepatic device with intrinsic microvascular-based channels, Biomed. Microdevices 10 (6) (2008) 795–805.
[67] Batchelor, G.K., An Introduction to Fluid Dynamics. Cambridge Mathematical Library. 2000, Cambridge: Cambridge University Press.
[68] P. Tabeling, Introduction to microfluidics, Oxford University Press, 2023.
[69] K. Kawata, et al., Mesenchymal cells and fluid flow stimulation synergistically regulate the kinetics of corneal epithelial cells at the air–liquid interface, Graefes Arch. Clin. Exp. Ophthalmol. 257 (9) (2019) 1915–1924.
[70] J.D. Humphrey, Vascular adaptation and mechanical homeostasis at tissue, cellular, and sub-cellular levels, Cell Biochem. Biophys. 50 (2) (2008) 53–78.
[71] Zhong, M., et al., Mechanosensing Piezo channels in tissue homeostasis including their role in lungs. Pulm Circ, 2018. 8(2): p. 2045894018767393.
[72] H. Rashidi, et al., Fluid shear stress modulation of hepatocyte-like cell function, Arch. Toxicol. 90 (7) (2016) 1757–1761.
[73] M. Uroz, et al., Regulation of cell cycle progression by cell–cell and cell–matrix forces, Nat. Cell Biol. 20 (6) (2018) 646–654.
[74] N. Azizipour, et al., Evolution of biochip technology: a review from lab-on-a-chip to organ-on-a-chip, Micromachines (Basel) 11 (6) (2020).
[75] T.M. Keenan, A. Folch, Biomolecular gradients in cell culture systems, Lab Chip 8 (1) (2008) 34–57.
[76] K. Lee, E.A. Silva, D.J. Mooney, Growth factor delivery-based tissue engineering: general approaches and a review of recent developments, J. R. Soc. Interface 8 (55) (2011) 153–170.
[77] Grushka, E. and E.J. Kikta Jr, Diffusion in liquids. II. The dependence of the diffusion coefficients on molecular weight and on temperature. Journal of the American Chemical Society, 1976. 98(3): p. 643-648.
[78] M. Schliwa, Action of cytochalasin D on cytoskeletal networks, J. Cell Biol. 92 (1) (1982) 79–91.
[79] J.F. Casella, M.D. Flanagan, S. Lin, Cytochalasin D inhibits actin polymerization and induces depolymerization of actin filaments formed during platelet shape change, Nature 293 (5830) (1981) 302–305.
[80] B.R. Stevenson, D.A. Begg, Concentration-dependent effects of cytochalasin D on tight junctions and actin filaments in MDCK epithelial cells, J. Cell Sci. 107 (3) (1994) 367–375.
[81] J.L. Bricker, S. Chu, S.A. Kempson, Disruption of F-actin stimulates hypertonic activation of the BGT1 transporter in MDCK cells, Am. J. Physiol.-Renal Physiol. 284 (5) (2003) F930–F937.
[82] Stankovic, m.,, et al., Quantification of structural changes in acute inflammation by fractal dimension, angular second moment and correlation, J. Microsc. 261 (3) (2016) 277–284.
[83] I. Pantic, et al., Nuclear entropy, angular second moment, variance and texture correlation of thymus cortical and medullar lymphocytes: grey level co-occurrence matrix analysis, An. Acad. Bras. Cienc. 85 (2013).
[84] T.S. Frost, et al., Permeability of epithelial/endothelial barriers in transwells and microfluidic bilayer devices, Micromachines 10 (8) (2019) 533.
[85] C.B. Goy, R.E. Chaile, R.E. Madrid, Microfluidics and hydrogel: a powerful combination, React. Funct. Polym. 145 (2019).